INRIA

INSTITUT NATIONAL DE RECHERCHE EN INFORMATIQUE ET EN AUTOMATIQUE

Numerical simulation of blood flows through a porous interface

M.A. Fernández — J.-F. Gerbeau — V. Martin

N° 6146

Mars 2007

Thème BIO

Rapport de recherche

ISSN 0249-6399 ISRN INRIA/RR--6146--FR+ENG

Numerical simulation of blood flows through a porous interface

M.A. Fernández[*†] , J.-F. Gerbeau[*‡] , V. Martin[*§]

Thème BIO — Systèmes biologiques
Projets Reo

Rapport de recherche n° 6146 — Mars 2007 — 30 pages

Abstract: We propose a model for a medical device, called a stent, designed for the treatment of cerebral aneurysms. The stent consists of a grid, immersed in the blood flow and located at the inlet of the aneurysm. It aims at promoting a clot within the aneurysm. The blood flow is modelled by the incompressible Navier-Stokes equations and the stent by a dissipative surface term. We propose a stabilized finite element method for this model and we analyse its convergence in the case of the Stokes equations. We present numerical results for academical test cases, and on a realistic aneurysm obtained from medical imaging.

Key-words: stabilized finite element, sieve problem, blood flow, terminal aneurysm, stent, fluid-structure interaction

1991 Mathematics Subject Classification: 65M60,74K25,76D05,76Z05

[*] Inria Rocquencourt, Reo Team, BP 105, 78153 Le Chesnay, France.
[†] Miguel.Fernandez@inria.fr.
[‡] Jean-Frederic.Gerbeau@inria.fr.
[§] University of Technology of Compiègne, LMAC, GI, Royallieu, BP 20529, 60205 Compiègne, France ; Vincent.Martin@utc.fr.

Unité de recherche INRIA Rocquencourt
Domaine de Voluceau, Rocquencourt, BP 105, 78153 Le Chesnay Cedex (France)
Téléphone : +33 1 39 63 55 11 —Télécopie : +33 1 39 63 53 30

Simulation numérique d'écoulements sanguins à travers une interface poreuse.

Résumé : Nous proposons un modèle pour un dispositif médical, appelé *stent*, destiné au traitement d'anévrismes cérébraux. Le stent consiste en une grille immergée dans l'écoulement sanguin à l'entrée de l'anévrisme. Son rôle est de favoriser la formation d'un caillot dans l'anévrisme. L'écoulement est modélisé par les équations de Navier-Stokes incompressible et le stent par un terme surfacique dissipatif. Nous proposons une méthode d'éléments finis stabilisés pour ce modèle et analysons sa convergence dans le cadre des équations de Stokes. Nous présentons des résultats de simulations sur des problèmes académiques et sur une géométrie réaliste d'anévrisme obtenue par imagerie médicale.

Mots-clés : éléments finis stabilisés, problème de passoire, écoulement sanguin, anévrisme terminal, stent, interaction fluide-structure

Introduction

This work is motivated by the numerical simulation of a new medical device[3] designed for the treatment of cerebral aneurysms located on bifurcations of arteries. This device consists of a wire metal mesh tube, called a *stent*. Contrary to the usual stents – which are typically used to keep arteries open and which are located on the vessel wall – this stent is immersed in the blood flow (Figure 1). The purpose of this device is to reduce the flux within the aneurysm in order to occlude it by a clot. For practical reasons, a portion of the stent is also present in front of collateral arteries, with a risk of adverse effect in the blood flows. The motivations of modelling are, first, quantify the desired reduction of vorticity and shear stress in the aneurysms and, second, the non-desired reduction of blood flows in collateral branches.

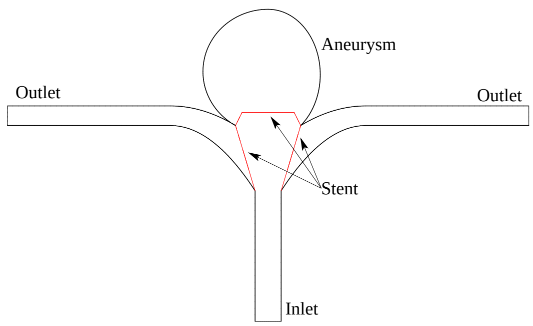

Figure 1: Example of a two-dimensional domain Ω with a stent ("LyLyk" device by Cardiatis) represented by a line γ. The part of the stent that lies on the arterial wall (vertical artery) is not represented.

For reasons that will be developed in Section 1, the geometrical details of the stent wires are ignored in this study. Our model thus consists in an homogenized porous interface immersed in the flow. From the mathematical standpoint, the flow is assumed to be governed by the incompressible Navier-Stokes equations and the stent is modelled by a dissipative surface term added to the left-hand side of the equations.

This additional dissipative term induces a jump of the stress across the stent surface which may raise numerical issues. On the one hand, continuous approximations of the pressure may give very inaccurate results, on the other hand, discontinuous approximations of the pressure typically lead to expensive simulations. To circumvent these issues, we propose to use stabilized finite elements, with continuous pressure, such as P_1/P_1 elements, and to introduce a "fissure" in the mesh on the stent surface, in order to allow for the pressure to be discontinuous *at the interface* only. The proposed stabilization formulation is made of two contributions: a standard residual based stabilization giving a L^2-control on the pressure gradient; an interface based stabilization providing a L^2-control on the jump of the pressure. In Section 2, a complete convergence analysis and an optimal error estimate are presented for the Stokes equations.

[3]The LyLyk© device, by Cardiatis.

Numerical results are presented in Section 3. The theoretical convergence rate of Section 2 is confirmed on an academical example where the solution is known in a closed-form. We also propose a validation test on a simple two dimensional configuration. We end the paper with results on realistic three dimensional geometries obtained from medical imaging. In that case, we also take into account the fluid-structure interaction of the blood with the wall artery.

1 Motivations and modelling

The purpose of the stent considered in this work is to treat intra-cranial terminal aneurysm located at an artery bifurcation (see *e.g.* [24]). Contrary to the stents commonly used to treat stenoses or side aneurysms, this stent is closed at one end. Moreover, it is characterized by very thin wires (40 μm), very small windows (100 μm) and a multilayer structure. It has the shape of a small, finely woven metallic socket, whose tip is intended to be inserted inside the aneurysm, whereas the sleeve would be in contact with the main artery. The part inside the aneurysm is finely braided, in order to reduce blood flow, and hopefully cause a thrombosis inside the aneurysm. The lateral part is more coarsely braided, in order to let the blood flow into the two daughter arteries.

In general, in finite element studies of stents in blood flows, each wire of the stent is meshed (see for instance [2, 25]). This approach requires an important work to generate the mesh, and is computationally heavy. Its interest is to provide a precise description of the local flow alterations caused by the stent. In our case, this approach is very expensive due to the very small windows of the stent and the complex multilayer structure. Moreover from the modelling viewpoint, it would be questionable to claim that one solves a resolution of 40 μm while neglecting the red blood cells (8μm diameter) which occupy about 50 % of the blood volume. This is why we preferred to model the stent "macroscopically" by a mean porous surface immersed in the flow. Note that we neglect any other physical aspects of the stent: deformation of its structure, interaction with the vessel wall, mechanical stability of the stent in the artery, *etc*.

Let Ω be a simply connected smooth domain in $\mathbb{R}^n$, $n = 2$ or 3, and $\Gamma = \partial\Omega$ its regular boundary. We suppose (see Figure 1) that the stent can be represented by a regular surface γ immersed in Ω.

Let $\mathbf{u}_f$ and p_f be the velocity and the pressure of the fluid. The strain rate tensor $\mathbf{D}$ and the Cauchy stress tensor $\mathbf{T}$ associated with $\mathbf{u}_f, p_f$ are defined by

$$\mathbf{D}(\mathbf{u}_f) = \frac{1}{2}\left(\nabla\mathbf{u}_f + \nabla\mathbf{u}_f^\top\right) \text{ and } \mathbf{T}(\mathbf{u}_f, p_f) = -p_f\mathbf{I} + 2\mu\mathbf{D}(\mathbf{u}_f),$$

where μ is the dynamic viscosity of the fluid, $\mathbf{u}_f$ is the velocity, p_f the pressure and $\mathbf{I}$ is the identity matrix in $\mathbb{R}^n$.

The blood is assumed to be governed by the incompressible Navier-Stokes equations. This is a commonly accepted hypothesis in the large vessels we are considering. To model the stent, we propose to add a dissipative surface term to the conservation of momentum equations. Thus, the model formally reads: find $\mathbf{u}_f$ and p_f such that

$$\begin{aligned} \rho_f\left(\frac{\partial\mathbf{u}_f}{\partial t} + \mathbf{u}_f\cdot\nabla\mathbf{u}_f\right) - \operatorname{div}\mathbf{T}(\mathbf{u}_f, p_f) + \mathbf{R}_\gamma\mathbf{u}\,\delta_\gamma &= \mathbf{f}_f \quad \text{in } \Omega, \\ \operatorname{div}\mathbf{u}_f &= 0 \quad \text{in } \Omega. \end{aligned} \tag{1}$$

where ρ_f is the density of the fluid, and $\mathbf{f}_f$ is the body force density, $\mathbf{R}_\gamma$ is a symmetric and positive definite tensor that represents the dissipation due to the stent, and δ_γ is the Dirac measure on the stent surface γ. In other words, for $\mathbf{v} \in [H^1(\Omega)]^n$,

$$\langle \mathbf{R}_\gamma \mathbf{u}_f \delta_\gamma, \mathbf{v} \rangle = \int_\gamma \mathbf{R}_\gamma \mathbf{u}_f \cdot \mathbf{v} \, d\gamma.$$

2 Numerical Analysis in the case of Stokes flows

In this section, the fluid is assumed to be governed by the stationary Stokes equations. For simplicity, we suppose (see Figure 2) that the stent is represented by a hyperplane γ that divides the domain Ω into two connected subdomains

$$\Omega_f = \Omega \backslash \gamma = \Omega_1 \cup \Omega_2, \qquad \Omega_1 \cap \Omega_2 = \emptyset.$$

We denote by $\mathbf{n_i}$ the outward normal on γ viewed as a part of the Ω_i boundary, for $i = 1, 2$. We

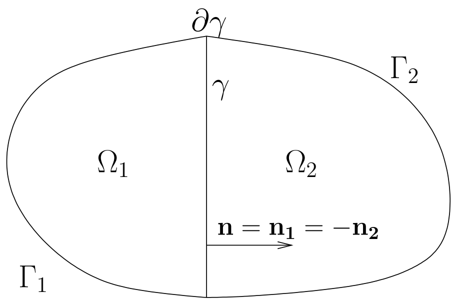

Figure 2: The domain Ω decomposed into two subdomains Ω_1 and Ω_2, separated by the stent γ.

denote by Γ_i the part of the boundary of Ω_i in common with the boundary of Ω:

$$\Gamma_i = \partial\Omega_i \cap \Gamma, \quad i = 1, 2.$$

We also introduce

$$\mathbf{u}_i = \mathbf{u}_f|_{\Omega_i}, \quad p_i = p_f|_{\Omega_i}, \quad \mathbf{f}_i = \mathbf{f}_f|_{\Omega_i}, \text{ for } i = 1, 2.$$

We will consider the usual Sobolev spaces $H^m(\mathcal{O})$, $m \geq 0$, for a given bounded open set $\mathcal{O} \subset \mathbb{R}^d$, $1 \leq d \leq n$. In particular, we have $L^2(\mathcal{O}) = H^0(\mathcal{O})$. The scalar product in $L^2(\mathcal{O})$ is denoted by $(\cdot,\cdot)_\mathcal{O}$ and its norm by $\|\cdot\|_{0,\mathcal{O}}$. The closed subspaces $H_0^1(\mathcal{O})$, consisting of functions in $H^1(\mathcal{O})$ with zero trace on $\partial\mathcal{O}$, and $L_0^2(\mathcal{O})$, consisting of function in $L^2(\mathcal{O})$ with zero mean in $\mathcal{O}$, will also be used. We define the following notations:

$$M = L^2(\Omega), \quad \tilde{M} = L_0^2(\Omega), \quad \mathbf{V} = [H_0^1(\Omega)]^n,$$

equipped with their usual norms $\|\cdot\|_{0,\Omega}$ and $\|\cdot\|_{1,\Omega}$. The subscript Ω will in general be omitted, when the norm is taken over the whole domain Ω. We assume that the right-hand side $\mathbf{f}_f \in [L^2(\Omega)]^n$.

2.1 Problem setting

The Stokes counterpart of problem (1) reads in a two-domain formulation:

$$\begin{aligned}
-\mu\Delta\mathbf{u}_i + \nabla p_i &= \mathbf{f}_i && \text{in } \Omega_i, \quad i=1,2,\\
\operatorname{div}\mathbf{u}_i &= 0 && \text{in } \Omega_i, \quad i=1,2,\\
\mathbf{u}_1 &= \mathbf{u}_2 && \text{on } \gamma,\\
\mu\nabla\mathbf{u}_1\cdot\mathbf{n}_1 - p_1\mathbf{n}_1 + \mu\nabla\mathbf{u}_2\cdot\mathbf{n}_2 - p_1\mathbf{n}_2 &= -\mathbf{R}_\gamma\mathbf{u} && \text{on } \gamma,\\
\mathbf{u}_i &= 0 && \text{on } \Gamma_i, \quad i=1,2,
\end{aligned} \tag{2}$$

where homogeneous Dirichlet boundary conditions on $\Gamma_i,\ i=1,2$ have been chosen for simplicity. Let $\mathbf{v}$ in $\mathbf{V}$ and $\mathbf{v}_i = \mathbf{v}|_{\Omega_i}, i=1,2$. Multiplying the first equations of (2) by $\mathbf{v}_i, i=1,2$, integrating by parts and adding the results, we readily obtain

$$\sum_{i=1}^{2}\Big[(\mu\nabla\mathbf{u}_i,\nabla\mathbf{v}_i)_{\Omega_i} - (p_i,\operatorname{div}\mathbf{v}_i)_{\Omega_i} - (\mu\nabla\mathbf{u}_i\cdot\mathbf{n}_i - p_i\mathbf{n}_i\,,\,\mathbf{v}_i)_\gamma\Big] \quad = \quad (\mathbf{f}_f,\mathbf{v})_\Omega\,. \tag{3}$$

Using $(2)_4$ and the regularity of $\mathbf{u}$ and $\mathbf{v}$, we obtain a variational formulation of problem (2): find $\mathbf{u}\in\mathbf{V}$ and $p\in\tilde{M}$ such that

$$\left\{\begin{aligned}
(\mu\nabla\mathbf{u},\,\nabla\mathbf{v})_\Omega + (\mathbf{R}_\gamma\mathbf{u},\,\mathbf{v})_\gamma - (\operatorname{div}\mathbf{v},\,p)_\Omega &= (\mathbf{f}_f,\,\mathbf{v})_\Omega && \forall\mathbf{v}\in\mathbf{V},\\
(\operatorname{div}\mathbf{u},\,r)_\Omega &= 0 && \forall r\in\tilde{M}.
\end{aligned}\right. \tag{4}$$

With the above assumptions on the data, we can state the following result.

Proposition 2.1. *Problem (4) has a unique solution.*

Proof. The result comes from the positivity of $\mathbf{R}_\gamma$ and a standard inf-sup condition (see [19]). □

Remark 2.2. Note that our heuristic model can be rigorously justified in some cases. Consider the 3D Stokes flow through a planar sieve made of a set of 2D obstacles, periodically spaced and identical and assume no-slip boundary conditions on the obstacles (see Figure 3).

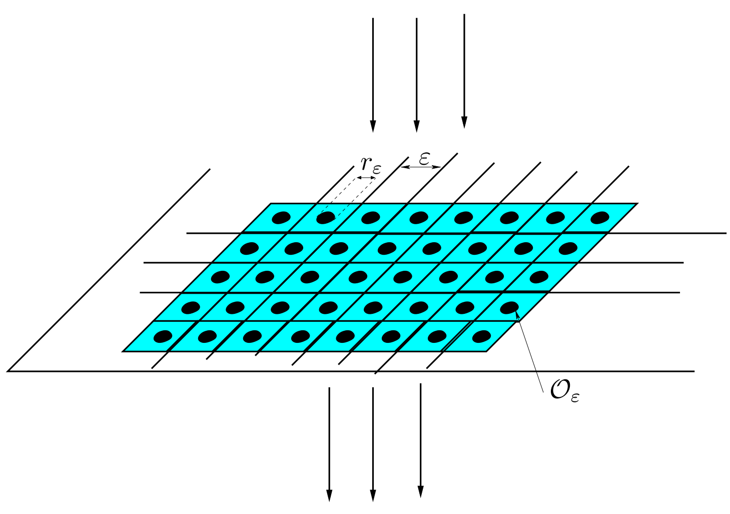

Figure 3: Planar Dirichlet sieve: regularly spaced obstacles where the flow is zero.

Then, three main asymptotic behaviors can be observed depending upon the limit $\alpha = \lim_{\varepsilon\to 0}(r_\varepsilon/\varepsilon^2)$ of the ratio of the radius r_ε of the obstacles over the square of the spatial periodicity ε:

- When $\alpha = 0$, the obstacles are asymptotically not seen by the flow: the limit problem is the Stokes problem in the whole domain.
- When $\alpha = +\infty$, the obstacles become asymptotically a wall, and the limit problem consists of two independent Stokes problems with no-slip condition on the interface.
- When $0 < \alpha < +\infty$, the limit problem is precisely (2). In that case, the resistivity tensor $\mathbf{R}_\gamma$ can be computed from a cell-problem defined on $\mathbb{R}^3\backslash O$, where O is the unit obstacle, and it can be proved that $\mathbf{R}_\gamma$ is symmetric positive definite.

We refer the interested reader to [1] and [4] for the proofs of these statements. The planar sieve has also been studied in [23, 10, 11].

2.2 Stabilized finite element approximation

The classical Galerkin method applied to (4) requires the fulfillment of a *inf-sup* condition [19] between the velocity and pressure spaces, which leads to formulations involving mixed interpolations [3]. From the computational point of view, it is more convenient to deal with equal order velocity-pressure interpolations, which requires that stability has to be enforced in another way. An approach consists in using *stabilized* finite element methods where some terms are added to the standard Galerkin formulation in order to enhance the stability of the method (see *e.g.* [20, 27, 9, 5]). For instance, in [20, 27] stability in achieved by adding a residual based term which gives L^2-control of the gradient of the pressure. Optimal error estimates, for arbitrary polynomial order $k \geq 1$, can be derived assuming that the solution is smooth enough, typically $(\mathbf{u}, p) \in [H^{k+1}(\Omega)]^n \times H^k(\Omega)$. In this work, we extend this approach to our specific situation.

It is important to notice that, due to the presence of the interface resistive term, one cannot expect more than $(\mathbf{u}, p) \in [H^1(\Omega)]^n \times L^2(\Omega)$ as global regularity of the solution of (4). As a result, some additional care have to be taken in order to approximate (4) by finite elements. On the other hand it seems reasonable to assume that

$$(\mathbf{u}_i, p_i) \in [H^{k+1}(\Omega_i)]^n \times H^k(\Omega_i), \quad i = 1, 2. \tag{5}$$

In this section, we propose a conforming stabilized finite element method, that allows equal order interpolations, and for which we can prove optimal error estimates under this reduced regularity. The key ingredient consists in combining the techniques of [20, 27] with an interface based stabilization allowing pressure discontinuities through the interface γ.

2.2.1 Preliminaries

In what follows, we shall assume Ω to be a Lipschitz-continuous domain in $\mathbb{R}^n$ ($n = 2$ or 3) with a polyhedral boundary $\partial\Omega$ and outward pointing normal $\mathbf{n}$. We shall also assume the viscosity μ to be constant. Let $\{\mathcal{T}_h\}_{0<h\leq 1}$ denotes a regular family of triangulations of the domain Ω (in the sense of [7]). For each triangulation $\mathcal{T}_h$, the subscript $h \in (0, 1]$ refers to the level of refinement of the triangulation, which is defined by

$$h = \max_{T\in\mathcal{T}_h} h_T,$$

with h_T, the diameter of T. We shall assume for the sake of simplicity the quasi-uniformity of the triangulation, *i.e.* there exist two positive constants $C_{\min}$ and $C_{\max}$ such that

$$C_{\min} h_T \leq h \leq C_{\max} h_T, \quad \forall T \in \mathcal{T}_h.$$

Moreover, for all $0 < h \leq 1$, the triangulation $\mathcal{T}_h$ is supposed to be conforming with the interface γ. Let $\mathcal{G}_h$ be the set of inter-element boundaries of $\mathcal{T}_h$ (faces in 3D, edges in 2D) lying on γ. For a given piecewise continuous function φ, the jump $[\![\varphi\mathbf{n}]\!]$ over an edge $E \in \mathcal{G}_h$ is defined by

$$[\![\varphi\mathbf{n}]\!](\mathbf{x}) = \lim_{t\to 0^+} \big(\varphi(\mathbf{x}+t\mathbf{n}_E^1)\mathbf{n}_E^1 + \varphi(\mathbf{x}+t\mathbf{n}_E^2)\mathbf{n}_E^2\big),$$

where $\mathbf{x} \in E$, and $\mathbf{n}_E^1$ (respectively $\mathbf{n}_E^2$) is the unit normal vector to E pointing outward Ω_1 (respectively outward Ω_2).

We consider equal order approximations of order $k \geq 1$ for the velocity and the pressure. Both velocity and pressure approximations will be continuous at inter-element boundaries, except for the pressure that will be discontinuous on the faces in 3D (on the edges in 2D) of the interface γ. Thus, we introduce the following velocity and pressure discrete spaces:

$$\begin{aligned} \mathbf{V}_h^k &= \big\{\mathbf{v}_h \in \mathcal{C}^0(\bar\Omega) \,:\, \forall T \in \mathcal{T}_h \ \mathbf{v}_h|_T \in (P_k)^n\big\} \cap \mathbf{V}, \\ M_h^k &= \Big\{q_h \in \tilde{M} \,:\, p|_{\Omega_i} \in \mathcal{C}^0(\bar\Omega_i), i=1,2, \quad \forall T \in \mathcal{T}_h \ q_h|_T \in P_k\Big\}. \end{aligned}$$

Finally, for $i = 1, 2$, let $M_{h,i}^k$ the space of the restrictions of elements of M_h^k to Ω_i,

$$M_{h,i}^k = \big\{q_{h|\Omega_i} \,:\, q_h \in M_h^k\big\}.$$

Let SZ_h^k be the Scott-Zhang interpolation operator onto $\mathbf{V}_h^k$ (see [13]). The following error estimate then holds,

$$\|\mathbf{u} - SZ_h^k\mathbf{u}\|_{0,\Omega} \leq c_0 h \|\mathbf{u}\|_{1,\Omega}. \tag{6}$$

In particular, using a trace inequality (see [8, 26]), we also have

$$\|\mathbf{u} - SZ_h^k\mathbf{u}\|_{0,E} \leq C_0 h^{1/2} \|\mathbf{u}\|_{1,\Omega}. \tag{7}$$

Let I_h^k be the Lagrange interpolation operator onto $\mathbf{V}_h^k$. Thus, we have the following estimates (see [13]), for $T \in \mathcal{T}_h$, and $0 \leq m \leq 2$, $2 \leq l \leq k+1$:

$$\|\mathbf{u} - I_h^k\mathbf{u}\|_{m,T} \leq c_1 h^{l-m} \|\mathbf{u}\|_{l,T} \quad \mathbf{u} \in [H^l(T)]^n. \tag{8}$$

Analogously, using a trace inequality, for $E \in \mathcal{G}_h$ $(E = T_1 \cap T_2,\ T_1, T_2 \in \mathcal{T}_h)$, we also have

$$\|\mathbf{u} - I_h^k\mathbf{u}\|_{0,E} \leq c_2 h^{l-1/2} \sum_{i=1,2} \|\mathbf{u}\|_{l,T_i} \quad \mathbf{u}|_{T_i} \in [H^l(T_i)]^n, i=1,2,\ \mathbf{u} \in [H^1(T_1 \cup T_2)]^n. \tag{9}$$

For $i = 1, 2$ let $J_{h,i}^k : L^2(\Omega_i) \mapsto M_{h,i}^k$ be the L^2-projection onto $M_{h,i}^k$. Thus, for $0 \leq m \leq 1$, $1 \leq l \leq k+1$, we have

$$\begin{aligned} \|p_i - J_{h,i}p_i\|_{m,\Omega_i} &\leq c_3 h^{l-m} \|p_i\|_{l,\Omega_i} \quad p_i \in H^l(\Omega_i), \\ \|p_i - J_{h,i}p_i\|_{0,\gamma} &\leq c_4 h^{l-1/2} \|p_i\|_{l,\Omega_i} \quad p_i \in H^l(\Omega_i). \end{aligned} \tag{10}$$

We then introduce the (global) operator $J_h^k : L^2(\Omega) \mapsto M_h^k$, defined by

$$(J_h^k p)|_{\Omega_i} = J_{h,i}^k(p|_{\Omega_i}), \quad i = 1, 2.$$

>From (10), it then follows that for $0 \leq m \leq 1$, $1 \leq l \leq k+1$,

$$\begin{aligned} &\|p - J_h^k p\|_{m,\Omega_i} \leq c_3 h^{l-m} \|p\|_{l,\Omega_i} \quad p \in L^2(\Omega),\ p|_{\Omega_i} \in H^l(\Omega_i),\ i=1,2, \\ &\|[\![p - J_h^k p]\!]\|_{0,\gamma} \leq c_4 h^{l-1/2} \sum_{i=1,2} \|p\|_{l,\Omega_i} \quad p \in L^2(\Omega),\ p|_{\Omega_i} \in H^l(\Omega_i),\ i=1,2. \end{aligned} \tag{11}$$

Using the quasi-uniformity of the mesh, the following inverse and trace estimates hold (see [13, 8]),

$$\|\Delta \mathbf{v}_h\|_{0,T} \leq c_5 h^{-1} \|\nabla \mathbf{v}_h\|_{0,T} \quad \mathbf{v}_h \in \mathbf{V}_h, \tag{12}$$

$$\|[\![\nabla \mathbf{v}_h \cdot \mathbf{n}]\!]\|_{0,E} \leq c_6 h^{-1/2} \|\mathbf{v}_h\|_{1,T_1 \cup T_2} \quad \mathbf{v}_h \in \mathbf{V}_h. \tag{13}$$

Finally, we also have the standard Sobolev trace inequality

$$\|\mathbf{u}|_\gamma\|_{0,\gamma} \leq c_\gamma \|\mathbf{u}\|_{1,\Omega} \quad \mathbf{u} \in \mathbf{V}.$$

2.2.2 A stabilized finite element method

Our finite element approximation for problem (4) reads: find $(\mathbf{u}_h, p_h) \in \mathbf{V}_h \times M_h$ such that

$$B_{\delta,\mathbf{R}_\gamma}\big((\mathbf{u}_h, p_h), (\mathbf{v}_h, q_h)\big) = F_\delta\big((\mathbf{v}_h, q_h)\big), \quad \forall (\mathbf{v}_h, q_h) \in \mathbf{V}_h \times M_h, \tag{14}$$

with

$$\begin{aligned} B_{\delta,\mathbf{R}_\gamma}\big((\mathbf{u}, p), (\mathbf{v}, q)\big) =& (\mu \nabla \mathbf{u},\, \nabla \mathbf{v})_\Omega + (\mathbf{R}_\gamma \mathbf{u},\, \mathbf{v})_\gamma - (p,\, \operatorname{div} \mathbf{v})_\Omega + (q,\, \operatorname{div} \mathbf{u})_\Omega \\ &+ \delta \sum_{T \in \mathcal{T}_h} \frac{h^2}{\mu} (-\mu \Delta \mathbf{u} + \nabla p,\, \nabla q)_T \\ &- \delta \sum_{E \in \mathcal{G}_h} \frac{h}{\mu} \big([\![\mu \nabla \mathbf{u} \cdot \mathbf{n} - p\mathbf{n}]\!] + \mathbf{R}_\gamma \mathbf{u}, [\![q\mathbf{n}]\!]\big)_E, \\ F_\delta\big((\mathbf{v}, q)\big) =& (\mathbf{f}_f, \mathbf{v})_\Omega + \delta \sum_{T \in \mathcal{T}_h} \frac{h^2}{\mu} (\mathbf{f}_f,\, \nabla q)_T\,, \end{aligned} \tag{15}$$

and $\delta > 0$ is a parameter independent of h and that will be determined in Theorem 2.8.

The stabilization is made of two contributions: a residual based stabilization [20, 27] giving a L^2-control on the pressure gradient, and an interface based stabilization providing L^2-control on the jumps of the pressure. Both stabilizing terms seem necessary to establish an inf-sup condition independent of the discretization parameter (see Proposition 2.5).

Assuming sufficient regularity of the solution, the discrete formulation (14) is strongly consistent. This is stated in following Proposition:

Proposition 2.3. *Assume that* $(\mathbf{u}, p) \in [H^1(\Omega)]^n \times L^2(\Omega)$, *the solution of* (14), *locally satisfies*

$$\begin{aligned} \mathbf{f}_f + \mu \Delta \mathbf{u} - \nabla p \in [L^2(T)]^n, &\quad \forall T \in \mathcal{T}_h, \\ [\![\mu \nabla \mathbf{u} \cdot \mathbf{n} - p\mathbf{n}]\!]_E + \mathbf{R}_\gamma \mathbf{u} \in [L^2(E)]^n, &\quad \forall E \in \mathcal{G}_h, \end{aligned}$$

and let $(\mathbf{u}_h, p_h) \in \mathbf{V}_h \times M_h$ *be the solution of* (14). *Then*

$$B_{\delta,\mathbf{R}_\gamma}\big((\mathbf{u} - \mathbf{u}_h, p - p_h), (\mathbf{v}_h, q_h)\big) = 0, \quad \forall (\mathbf{v}_h, q_h) \in \mathbf{V}_h \times M_h. \tag{16}$$

Proof. It is a direct consequence of the strong consistency of the standard Galerkin method, the fact that the solution satisfies

$$\begin{aligned} \mathbf{f}_f + \mu \Delta \mathbf{u} - \nabla p = 0, &\quad \text{in} \quad [\mathcal{D}'(\Omega_i)]^n, \quad i=1,2, \\ [\![\mu \nabla \mathbf{u} \cdot \mathbf{n} - p\mathbf{n}]\!]_\gamma + \mathbf{R}_\gamma \mathbf{u} = 0, &\quad \text{in} \quad [H^{-1/2}(\gamma)]^n, \end{aligned}$$

and the γ-conformity of the triangulation $\mathcal{T}_h$. □

2.2.3 Stability

In what follows we assume that there exist two positive constants $r_{\min}$ and $r_{\min}$ such that

$$r_{\min}|\mathbf{y}|^2 \leq \mathbf{y}^{\mathrm{T}}\mathbf{R}_\gamma(\mathbf{x})\mathbf{y} \leq r_{\max}|\mathbf{y}|^2, \quad \forall \mathbf{x} \in \gamma, \quad \forall \mathbf{y} \in \mathbb{R}^n. \tag{17}$$

The convergence of the discrete solution will be stated in terms of the following mesh-dependent norm on $\mathbf{V}_h \times M_h$:

$$|\!|\!|(\mathbf{u},p)|\!|\!|_h^2 = |\mu^{1/2}\mathbf{u}|_{1,\Omega}^2 + \|r_{\min}^{1/2}\mathbf{u}\|_{0,\gamma}^2 + \delta \sum_{T\in\mathcal{T}_h} \frac{h^2}{\mu}\|\nabla p\|_{0,T}^2 + \delta \sum_{E\in\mathcal{G}_h} \frac{h}{\mu}\|[\![p]\!]\|_{0,E}^2 + \|\mu^{-1/2}p\|_{0,\Omega}^2, \tag{18}$$

for all $(\mathbf{u},p) \in \mathbf{V}_h \times M_h$.

The following result states the coercivity of our discrete operator with respect to a weaker norm than the mesh-dependent norm.

Proposition 2.4. *Assume that*

$$0 < \delta \leq \frac{1}{c_5^2 + 2c_6^2}, \quad \delta h \leq \frac{\mu\, r_{\min}}{2\, r_{\max}^2}. \tag{19}$$

Then

$$B_{\delta,\mathbf{R}_\gamma}\big((\mathbf{u}_h,p_h),(\mathbf{u}_h,p_h)\big) \geq \frac{1}{2}\left(|\!|\!|(\mathbf{u}_h,p_h)|\!|\!|_h^2 - \|\mu^{-1/2}p_h\|_{0,\Omega}^2\right),$$

for all $(\mathbf{u}_h,p_h) \in \mathbf{V}_h \times M_h$.

Proof. Using the definition of $B_{\delta,\mathbf{R}_\gamma}$ and the notations

$$x = \left\{\delta \sum_{T\in\mathcal{T}_h} \frac{h^2}{\mu}\|\nabla p_h\|_T^2\right\}^{1/2}, \quad y = \left\{\delta \sum_{E\in\mathcal{G}_h} \frac{h}{\mu}\|[\![p_h]\!]\|_E^2\right\}^{1/2}, \tag{20}$$

we have

$$\begin{aligned} B_{\delta,\mathbf{R}_\gamma}\big((\mathbf{u}_h,p_h),(\mathbf{u}_h,p_h)\big) \geq & |\mu^{1/2}\mathbf{u}_h|_{1,\Omega}^2 + \|r_{\min}^{1/2}\mathbf{u}_h\|_{0,\gamma}^2 + x^2 + y^2 + \delta \sum_{T\in\mathcal{T}_h} h^2(-\Delta\mathbf{u}_h,\, \nabla p_h)_T \\ & + \delta \sum_{E\in\mathcal{G}_h} \frac{h}{\mu}([\![\mu\nabla\mathbf{u}_h\cdot\mathbf{n}]\!] + \mathbf{R}_\gamma\mathbf{u}_h,\, -[\![p_h\mathbf{n}]\!])_E. \end{aligned}$$

Using the inverse estimates (12) and (13), it follows that

$$\begin{aligned} B_{\delta,\mathbf{R}_\gamma}\big((\mathbf{u}_h,p_h),(\mathbf{u}_h,p_h)\big) \geq & |\mu^{1/2}\mathbf{u}_h|_{1,\Omega}^2 + \|r_{\min}^{1/2}\mathbf{u}_h\|_{0,\gamma}^2 + x^2 + y^2 - \delta^{1/2}c_5(\mu|\mathbf{u}_h|_{1,\Omega}^2)^{1/2}\, x \\ & - \delta^{1/2}c_6(\mu|\mathbf{u}_h|_{1,\Omega}^2)^{1/2}\, y - \left(\delta\frac{r_{\max}^2 h}{r_{\min}\mu}\right)^{1/2} \|r_{\min}^{1/2}\mathbf{u}_h\|_{0,\gamma}\, y \\ \geq & \left[1 - \delta\left(\frac{c_5^2}{2} + c_6^2\right)\right] |\mu^{1/2}\mathbf{u}_h|_{1,\Omega}^2 + \left(1 - \delta\frac{r_{\max}^2 h}{r_{\min}\mu}\right) \|r_{\min}^{1/2}\mathbf{u}_h\|_{0,\gamma}^2 \\ & + \frac{1}{2}x^2 + \frac{1}{2}y^2. \end{aligned}$$

Finally, using (19), we get

$$B_{\delta,\mathbf{R}_\gamma}\big((\mathbf{u}_h,p_h),(\mathbf{u}_h,p_h)\big) \geq \frac{1}{2}\left\{|\mu^{1/2}\mathbf{u}_h|_{1,\Omega}^2 + \|r_{\min}^{1/2}\mathbf{u}_h\|_{0,\gamma}^2 + x^2 + y^2\right\}, \tag{21}$$

which concludes the proof. □

Now we state the main stability result for our method. This is the aim of the following theorem:

Theorem 2.5. *Under the hypotheses of Proposition* 2.4*, there exists a constant* $\beta = \beta(\delta, r_{\min}, r_{\max}, \mu) > 0$ *such that*

$$\inf_{(\mathbf{u}_h,p_h)\in\mathbf{V}_h\times M_h}\ \sup_{(\mathbf{v}_h,q_h)\in\mathbf{V}_h\times M_h} \frac{B_{\delta,\mathbf{R}_\gamma}\big((\mathbf{u}_h,p_h),\,(\mathbf{v}_h,q_h)\big)}{|||(\mathbf{u}_h,p_h)|||_h\,|||(\mathbf{v}_h,q_h)|||_h} \geq \beta.$$

Moreover, $\beta = \mathcal{O}(\delta)$*, if* $\delta \ll 1$*, and* $\beta = \mathcal{O}\left(\frac{\mu}{r_{\min}}\right)$*, if* $\frac{r_{\min}}{\mu} \gg 1$.

Proof. Let $(\mathbf{u}_h, p_h) \in \mathbf{V}_h \times M_h$. There exists a $\mathbf{v} \in \mathbf{V}$ and a constant c_Ω, which only depends on Ω, such that $\mathrm{div}\mathbf{v} = -p_h$ and $\|\mathbf{v}\|_{1,\Omega} \leq c_\Omega \|p_h\|_{0,\Omega}$, see for instance [19]. Let $\mathbf{v}_h = SZ_h^k \mathbf{v}$. Using the H^1-stability of SZ_h^k (see [13]) we have $\|\mathbf{v}_h\|_{1,\Omega} \leq c'_\Omega \|p_h\|_{0,\Omega}$.

Using partial integration element-wise and the continuity of p_h in Ω_1 and Ω_2, one obtains

$$\begin{aligned} B_{\delta,\mathbf{R}_\gamma}\big((\mathbf{u}_h,p_h),(\mathbf{v}_h,0)\big) =& (\mu\nabla\mathbf{u}_h,\,\nabla\mathbf{v}_h)_\Omega + (\mathbf{R}_\gamma\mathbf{u}_h,\,\mathbf{v}_h)_\gamma - (p_h,\,\mathrm{div}\mathbf{v})_\Omega \\ & - \sum_{T\in\mathcal{T}_h} (\nabla p_h,\,\mathbf{v}-\mathbf{v}_h)_T + \sum_{E\in\mathcal{G}_h} ([\![p_h\mathbf{n}]\!],\,\mathbf{v}-\mathbf{v}_h)_E. \end{aligned}$$

Therefore, using Cauchy-Schwarz and approximation (6)-(7), one obtains

$$\begin{aligned} B_{\delta,\mathbf{R}_\gamma}\big((\mathbf{u}_h,p_h),(\mathbf{v}_h,0)\big) \geq& \|p_h\|_{0,\Omega}^2 - |\mu^{1/2}\mathbf{u}_h|_{1,\Omega}\,|\mu^{1/2}\mathbf{v}_h|_{1,\Omega} - \frac{r_{\max}}{r_{\min}^{1/2}}\|r_{\min}^{1/2}\mathbf{u}_h\|_{0,\gamma}\|\mathbf{v}_h\|_{0,\gamma} \\ & - \left[c_0\left(\sum_{T\in\mathcal{T}_h} h^2\|\nabla p_h\|_{0,T}^2\right)^{1/2} + C_0\left(\sum_{E\in\mathcal{G}_h} h\|[\![p_h]\!]\|_{0,E}^2\right)\right]\|\mathbf{v}\|_{1,\Omega}. \end{aligned}$$

It then follows that

$$\begin{aligned} B_{\delta,\mathbf{R}_\gamma}\big((\mathbf{u}_h,p_h),(\mathbf{v}_h,0)\big) \geq& \|p_h\|_{0,\Omega}^2 - c'_\Omega\mu^{1/2}|\mu^{1/2}\mathbf{u}_h|_{1,\Omega}\|p_h\|_{0,\Omega} - c'_\Omega c_\gamma \frac{r_{\max}}{r_{\min}^{1/2}}\|r_{\min}^{1/2}\mathbf{u}_h\|_{0,\gamma}\|p_h\|_{0,\Omega} \\ & - \left(\frac{\mu}{\delta}\right)^{1/2} c_0 c_\Omega\, x\,\|p_h\|_{0,\Omega} - \left(\frac{\mu}{\delta}\right)^{1/2} C_0 c_\Omega\, y\,\|p_h\|_{0,\Omega} \\ \geq& \|p_h\|_{0,\Omega}^2 - c_\delta\mu^{1/2}\left(|\mu^{1/2}\mathbf{u}_h|_{1,\Omega} + \|r_{\min}^{1/2}\mathbf{u}_h\|_{0,\gamma} + x + y\right)\|p_h\|_{0,\Omega} \\ \geq& \frac{1}{2}\|p_h\|_{0,\Omega}^2 - 2c_\delta^2\mu\left(|\mu^{1/2}\mathbf{u}_h|_{1,\Omega}^2 + \|r_{\min}^{1/2}\mathbf{u}_h\|_{0,\gamma}^2 + x^2 + y^2\right), \end{aligned} \tag{22}$$

where

$$c_\delta = \max\left\{c'_\Omega,\ c'_\Omega c_\gamma \frac{r_{\max}}{\mu^{1/2} r_{\min}^{1/2}},\ \delta^{-1/2}c_0 c_\Omega,\ \delta^{-1/2}C_0 c_\Omega\right\}.$$

Multiply (21) by $(1-\rho)$ and (22) by ρ, and add the resulting results to obtain

$$\begin{aligned} B_{\delta,\mathbf{R}_\gamma}\Big((\mathbf{u}_h,p_h),\,((1-\rho)\mathbf{u}_h + \rho\mathbf{v}_h,(1-\rho)p_h)\Big) &= (1-\rho)B_{\delta,\mathbf{R}_\gamma}\Big((\mathbf{u}_h,p_h),\,(\mathbf{u}_h,p_h)\Big) \\ + \rho\Big((\mathbf{u}_h,p_h),\,(\mathbf{v}_h,0)\Big) &\geq \left(\frac{1-\rho}{2} - 2\rho c_\delta^2\mu\right)\left(\mu|\mathbf{u}_h|_1^2 + \|(r_{\min})^{1/2}\mathbf{u}\|_{0,\gamma}^2 + x^2 + y^2\right) \\ & \quad + \frac{\rho\mu}{2}\|\mu^{-1/2}p_h\|_{0,\Omega}^2. \end{aligned}$$

So that, if we take

$$0 < \rho = \frac{1}{1 + 4c_\delta^2 \mu + \mu} < 1,$$

we then obtain that

$$B_{\delta,\mathbf{R}_\gamma}\Big((\mathbf{u}_h, p_h), ((1-\rho)\mathbf{u}_h + \rho \mathbf{v}_h, (1-\rho)p_h)\Big) \geq \frac{\mu}{2 + 8c_\delta^2\mu + 2\mu} \| (\mathbf{u}_h, p_h) \|_h^2. \tag{23}$$

Moreover,

$$\begin{aligned}
\Big\| \Big((1-\rho)\mathbf{u}_h + \rho\mathbf{v}_h, (1-\rho)p_h\Big) \Big\|_h &\leq (1-\rho) \|(\mathbf{u}_h, p_h)\|_h + \rho \|(\mathbf{v}_h, 0)\|_h \\
&\leq (1-\rho)\, \|(\mathbf{u}_h, p_h)\|_h + \rho \left\{ \mu |\mathbf{v}_h|_{1,\Omega}^2 + \| r_{\min}^{1/2} \mathbf{v}_h \|_{0,\gamma}^2 \right\}^{1/2} \\
&\leq (1-\rho)\, \|(\mathbf{u}_h, p_h)\|_h + \rho\sqrt{2}\, c_\delta \mu \, \| \mu^{-1/2} p_h \|_{0,\Omega} \\
&\leq \mu \frac{1 + \sqrt{2}\, c_\delta + 4c_\delta^2}{1 + 4c_\delta^2 \mu + \mu} \, \|(\mathbf{u}_h, p_h)\|_h.
\end{aligned} \tag{24}$$

Combining (23) and (24), one obtains the desired inf-sup estimation with

$$\beta = \frac{1}{2 + 2\sqrt{2}\, \mu^{1/2} c_\delta + 8c_\delta^2}.$$

The asymptotic behavior of β follows from this equation and the definition of c_δ, so the proof is complete. □

As a direct consequence of the previous result, we have the following corollary.

Corollary 2.6. *There exists a unique solution to problem (14).*

2.2.4 Convergence analysis

In this paragraph we provide an optimal error estimate under the reduced regularity assumptions (5). First, we prove the following approximability result with respect to the mesh-dependent norm $\|\cdot\|_h$.

Proposition 2.7. *Assume that $(\mathbf{u}, p)$ satisfies (5). Then, there exists a positive constant c, independent of h and the physical parameters, such that:*

$$\|(\mathbf{u} - I_h^k \mathbf{u}, p - J_h^k p)\|_h \leq c(\beta)\, h^k \left[\left(\mu^{1/2} + r_{\min}^{1/2} h^{1/2} \right) \mathcal{N}_{k+1}(\mathbf{u}) + (1 + \delta^{1/2}) \mu^{-1/2} \mathcal{N}_k(p) \right],$$

with the notations

$$\mathcal{N}_{k+1}(\mathbf{u}) = \sum_{i=1,2} \|\mathbf{u}\|_{k+1,\, \Omega_i}, \quad \mathcal{N}_k(p) = \sum_{i=1,2} \|p\|_{k,\, \Omega_i}.$$

Proof. Using the definition (18) and the approximation properties of I_h^k and J_h^k (8) and (11), we have

$$
\begin{aligned}
\|\!|(\mathbf{u}-I_h^k\mathbf{u}, p-J_h^k p)\|\!|_h =& \Big\{|\mu^{1/2}(\mathbf{u}-I_h^k\mathbf{u})|_{1,\Omega}^2 + \|\mu^{-1/2}(p-J_h^k p)\|_{0,\Omega}^2 + \|r_{\min}^{1/2}(\mathbf{u}-I_h^k\mathbf{u}_h)\|_{0,\gamma}^2 \\
&+ \delta\frac{h^2}{\mu}\sum_{i=1,2}\|\nabla(p-J_h^k p)\|_{0,\Omega_i}^2 + \delta\frac{h}{\mu}\|[\![p-J_h^k p]\!]\|_{0,\gamma}^2\Big\}^{1/2} \\
\leq& \left(c_1\mu^{1/2}h^k + c_2 r_{\min}^{1/2}h^{k+1/2}\right)\mathcal{N}_{k+1}(\mathbf{u}) \\
&+ \left(c_3\,\mu^{-1/2}h^k + \delta^{1/2}\mu^{-1/2}(c_3+c_4)\,h^k\right)\mathcal{N}_k(p) \\
\leq& c\,h^k\left[\left(\mu^{1/2}+r_{\min}^{1/2}h^{1/2}\right)\mathcal{N}_{k+1}(\mathbf{u}) + \left(\mu^{-1/2}+\delta^{1/2}\mu^{-1/2}\right)\mathcal{N}_k(p)\right],
\end{aligned}
$$

which completes the proof. □

The main result of this paragraph is stated in the next theorem.

Theorem 2.8. *Let $(\mathbf{u},p)\in\mathbf{V}\times\tilde{M}$ be the solution of problem (4), and $(\mathbf{u}_h,p_h)\in\mathbf{V}_h\times M_h$ the solution of problem (14). Assume that $(\mathbf{u},p)$ satisfies the regularity assumptions (5) and that the hypotheses of Proposition 2.3 and 2.4 hold. Then, there exists a positive constant c, independent of h, depending on the inf-sup constant β, such that*

$$
\begin{aligned}
&\|\!|(\mathbf{u}-\mathbf{u}_h, p-p_h)\|\!|_h \\
\leq\;& c(\beta)\,h^k\Bigg\{\left(\mu^{1/2}+\delta^{1/2}\mu^{1/2}+\delta^{-1/2}\mu^{1/2}+\frac{r_{\max}}{r_{\min}^{1/2}}\,h^{1/2}+\delta^{1/2}\mu^{-1/2}r_{\max}\,h\right)\sum_{i=1,2}\|\mathbf{u}\|_{k+1,\,\Omega_i} \\
&+\left(\mu^{-1/2}+\delta^{1/2}\mu^{-1/2}\right)\sum_{i=1,2}\|p\|_{k,\,\Omega_i}\Bigg\}
\end{aligned}
$$

Proof. Take the interpolants $\mathbf{v}_h = I_h^k\mathbf{u}$ and $q_h = J_h^k p$. Decompose the error into the interpolation and approximation errors,

$$
\|\!|(\mathbf{u}-\mathbf{u}_h, p-p_h)\|\!|_h \leq \|\!|(\mathbf{u}-\mathbf{v}_h, p-q_h)\|\!|_h + \|\!|(\mathbf{u}_h-\mathbf{v}_h, p_h-q_h)\|\!|_h.
$$

The first term can be bounded using Proposition 2.7, so we only need to estimate $\|\!|(\mathbf{u}_h-\mathbf{v}_h, p_h-q_h)\|\!|_h$. Using the inf-sup condition (Propositions 2.5) and the Galerkin orthogonality (16), we have

$$
\begin{aligned}
\|\!|(\mathbf{u}_h-\mathbf{v}_h, p_h-q_h)\|\!|_h \;&\leq\; \frac{1}{\beta}\sup_{(\mathbf{w}_h,r_h)\in\mathbf{V}_h\times M_h}\frac{B_{\delta,\mathbf{R}_\gamma}\big((\mathbf{u}_h-\mathbf{v}_h, p_h-q_h),\,(\mathbf{w}_h,r_h)\big)}{\|\!|(\mathbf{w}_h,r_h)\|\!|_h} \\
&\leq\; \frac{1}{\beta}\sup_{(\mathbf{w}_h,r_h)\in\mathbf{V}_h\times M_h}\frac{B_{\delta,\mathbf{R}_\gamma}\big((\mathbf{u}-\mathbf{v}_h, p-q_h),\,(\mathbf{w}_h,r_h)\big)}{\|\!|(\mathbf{w}_h,r_h)\|\!|_h}.
\end{aligned}
$$

To estimate the right-hand side of the above inequality, we take $(\mathbf{w}_h,r_h)\in\mathbf{V}_h\times M_h$ arbitrarily, and we bound separately each term of $B_{\delta,\mathbf{R}_\gamma}\big((\mathbf{u}-\mathbf{v}_h, p-q_h),\,(\mathbf{w}_h,r_h)\big)$, using approximation estimates (8) and (11). For the viscous term, we have

$$
(\mu\nabla(\mathbf{u}-\mathbf{v}_h),\,\nabla\mathbf{w}_h)_\Omega \leq c_1\,h^k\mu^{1/2}\,\mathcal{N}_{k+1}(\mathbf{u})\|\!|(\mathbf{w}_h,r_h)\|\!|_h.
$$

The resistive term is treated as follows

$$
\begin{aligned}
(\mathbf{R}_\gamma(\mathbf{u}-\mathbf{v}_h),\, \mathbf{w}_h)_\gamma &\leq \|{\mathbf{R}_\gamma}^{1/2}(\mathbf{u}-\mathbf{v}_h)\|_{0,\gamma}\|{\mathbf{R}_\gamma}^{1/2}\mathbf{w}_h\|_{0,\gamma}\\
&\leq c_2 \frac{r_{\max}}{r_{\min}^{1/2}}\, h^{k+1/2}\, \mathcal{N}_{k+1}(\mathbf{u}) |\!|\!|(\mathbf{w}_h, r_h)|\!|\!|_h.
\end{aligned}
$$

For the pressure term, we have

$$
-(p-q_h,\, \mathrm{div}\mathbf{w}_h)_\Omega \leq c_3\, \mu^{-1/2} h^k\, \mathcal{N}_k(p)\, \sqrt{n} |\!|\!|(\mathbf{w}_h, r_h)|\!|\!|_h.
$$

By integration by parts, we obtain

$$
\begin{aligned}
(r_h,\, \mathrm{div}(\mathbf{u}-\mathbf{v}_h)_\Omega &= -\sum_{T\in\mathcal{T}_h} (\nabla r_h,\, \mathbf{u}-\mathbf{v}_h)_T + \sum_{E\in\mathcal{G}_h} (\mathbf{u}-\mathbf{v}_h,\, [\![r_h \mathbf{n}]\!])_E\\
&\leq (c_1+c_2)\, h^k\, \mathcal{N}_{k+1}(\mathbf{u})\; \delta^{-1/2}\mu^{1/2} |\!|\!|(\mathbf{w}_h, r_h)|\!|\!|_h.
\end{aligned}
$$

For the stabilization terms, we have

$$
\begin{aligned}
&\delta \sum_{T\in\mathcal{T}_h} \frac{h^2}{\mu}\, (-\mu\Delta(\mathbf{u}-\mathbf{v}_h) + \nabla(p-q_h),\, \nabla r_h)_T\\
&\qquad\leq h^k\, \Big(c_1\, \delta^{1/2}\mu^{1/2}\, \mathcal{N}_{k+1}(\mathbf{u}) \; + c_3\, \delta^{1/2}\mu^{-1/2}\, \mathcal{N}_k(p) \Big) |\!|\!|(\mathbf{w}_h, r_h)|\!|\!|_h.
\end{aligned}
$$

On the other hand, using the fact that $\nabla\mathbf{u} \in H^k(\Omega_i)^{n\times n}, i=1,2$ and since

$$
\|[\![\nabla(\mathbf{u}-\mathbf{v}_h)\cdot\mathbf{n}]\!]\|_{0,E} \leq \|[\![\nabla(\mathbf{u}-\mathbf{v}_h)]\!]\|_{0,E} \leq c_2\, h^{k-1/2} \sum_{i=1,2} \|\nabla\mathbf{u}\|_{k,\,T_i}, \quad E = T_1\cap T_2,
$$

we obtain

$$
\begin{aligned}
\delta \sum_{E\in\mathcal{G}_h} \frac{h}{\mu}\, ([\![\mu\nabla(\mathbf{u}-\mathbf{v}_h)\cdot\mathbf{n}]\!], -[\![r_h\mathbf{n}]\!])_E &\leq c_2\, h^k\, \delta^{1/2}\mu^{1/2}\, \mathcal{N}_{k+1}(\mathbf{u})\; |\!|\!|(\mathbf{w}_h, r_h)|\!|\!|_h,\\
\delta \sum_{E\in\mathcal{G}_h} \frac{h}{\mu}\, (\mathbf{R}_\gamma(\mathbf{u}-\mathbf{v}_h),\, -[\![r_h\mathbf{n}]\!])_E &\leq c_2\, h^{k+1}\, \delta^{1/2}\mu^{-1/2} r_{\max}\, \mathcal{N}_{k+1}(\mathbf{u})\; |\!|\!|(\mathbf{w}_h, r_h)|\!|\!|_h,\\
\delta \sum_{E\in\mathcal{G}_h} \frac{h}{\mu}\, ([\![-(p-q_h)\mathbf{n}]\!],\, -[\![r_h\mathbf{n}]\!])_E &\leq c_4\, h^k\, \delta^{1/2}\mu^{-1/2}\, \mathcal{N}_k(p)\; |\!|\!|(\mathbf{w}_h, r_h)|\!|\!|_h.
\end{aligned}
$$

We conclude the proof by summing up all the contributions. □

3 Numerical results

This section is devoted to numerical results. In Section 3.1, we assess the theoretical convergence rates stated in Section 2.2 with an analytical test-case. In Section 3.2, we consider a quasi-Poiseuille flow through a porous surface using different discretization spaces. The purpose is to stress the relevance of using discontinuous pressures across the interface and to show that the proposed stabilized finite element provides solutions similar to those obtained with more expensive finite elements. Finally, in Section 3.3, we show the results of simulations with a realistic aneurysm geometry, both with rigid and elastic walls.

3.1 Assessment of the convergence rate

We build an analytical solution of the problem in order to assess the convergence rate proved above. Let $\Omega = (0,2) \times (0,1)$ be the fluid domain divided in two subdomains $\Omega_1 = (0,L) \times (0,1)$ and $\Omega_1 = (L,2) \times (0,1)$, by the interface $\gamma = \{L\} \times (0,1)$, where $L = 1$. Assume that the viscosity $\mu = 0.04$ and the resistivity is the scalar matrix $\mathbf{R}_\gamma = 100\ \mathbf{I}$. We compute $\mathbf{f}_f$ and the non-homogeneous boundary conditions such that the following functions are solution to problem (2):

$$\mathbf{u}^1 = \left[\begin{array}{c} -19.98\ x + 10\ x^2 \\ -40.04 + 19.98\ y + 40\ x^2 - 20\ xy \end{array} \right], \ \mathbf{u}^2 = \left[\begin{array}{c} 25\ x - 69.98\ x + 35\ x^2 \\ 9.96 + 69.98\ y - 10\ x^2 - 70\ xy \end{array} \right],$$

and

$$p^1 = 800, \ p^2 = 998 + 800\ y^2,$$

where $(\mathbf{u}^i, p^i)$ denotes the solution in Ω_i. This solution is depicted in Figure 4.

Various unstructured triangulations with decreasing mesh parameters $h \in \{1/10; 1/20; 1/40; 1/80\}$ have been considered and the results are reported in Figure 5. The relative errors in velocity $\left(\dfrac{||\mathbf{u} - \mathbf{u}_h||_0}{||\mathbf{u}||_0}\right)$ and pressure $\left(\dfrac{||p - p_h||_0}{||p||_0}\right)$ show an almost quadratic convergence in h with the stabilization introduced in Section 2.2. This is in agreement with our analysis. For the gradient of the velocity, we observe a convergence rate which is better than expected. This might be related to the particular test case at hand. A comparison with the "classical" residual based stabilizations (Fig. 5, left), namely without interface stabilization terms, show that the proposed stabilization method performs similarly as far as the velocity is concerned, but enjoys a better convergence rate for the pressure. This property, predicted by the theoretical analysis, is one of the main motivations of the proposed method.

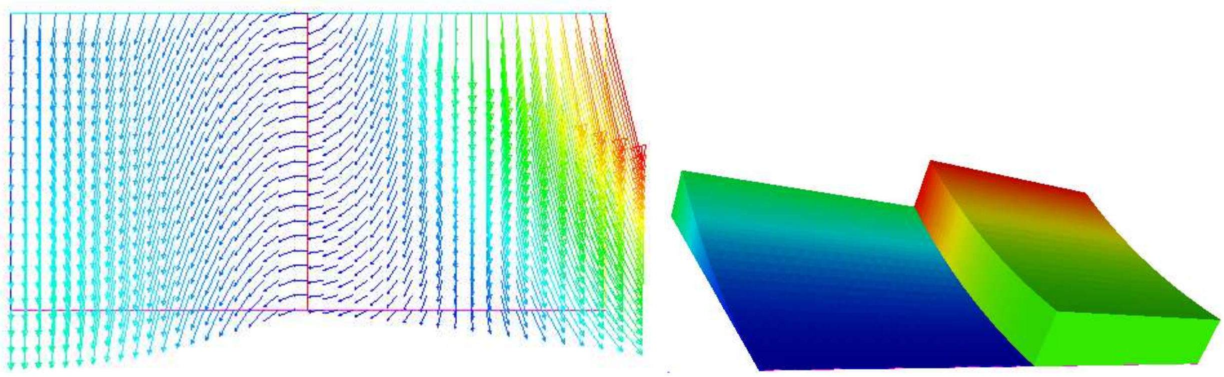

Figure 4: Velocity (left) and pressure (right) with a resistive stent (red vertical line, $r_\gamma = 100$) corresponding to the Section 3.1 test-case. Discretization: P_1/P_1 with a fissure. Velocity scale: from 9.63 up to 103.1. Pressure scale: from 0 up to 1800. The mesh presented in this figure is quite coarse for clarity

3.2 Quasi-Poiseuille flow

3.2.1 Description of the problem

We consider a 2D stationary flow in a straight 2D tube of length $L = L_1 + L_2$, $L_1 > 0$ and $L_2 > 0$, of width $2b > 0$, with a stent γ located inside the tube, see Figure 6. We decomposed the domain

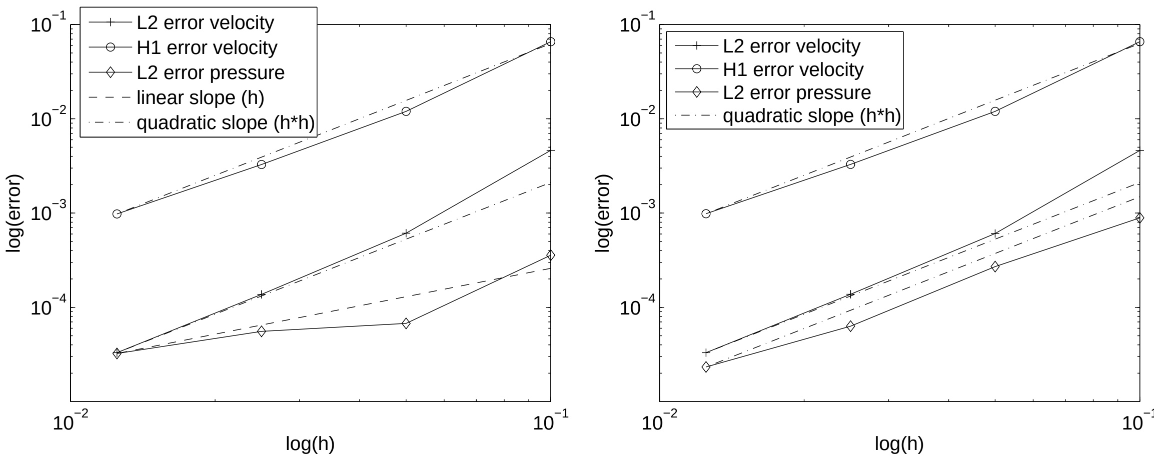

Figure 5: Test-case of Section 3.1. Relative error as a function of the discretization step h, in log scales. Left: classical residual based stabilization. Right: stabilization of Section 2.2.

$\Omega = (0, L) \times (-b, b)$ into two subdomains $\Omega_1 = (0, L_1) \times (-b, b)$ and $\Omega_2 = (L_1, L) \times (-b, b)$. The stent is modeled by a resistivity $\mathbf{R}_\gamma = r_\gamma \mathbf{I}$ at the interface $\gamma = \{L_1\} \times (-b, b)$.

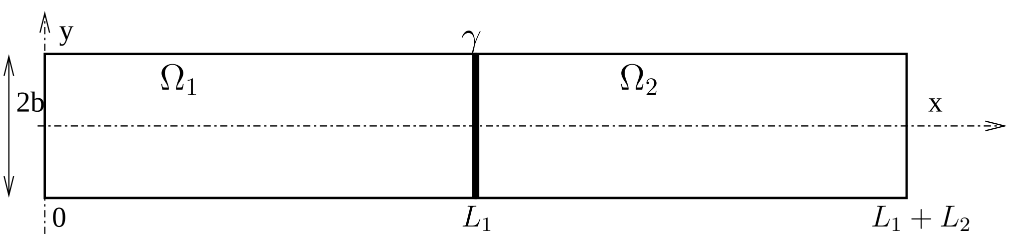

Figure 6: Quasi-Poiseuille test-case: the subdomains Ω_1 and Ω_2 are separated by the stent considered as a straight line γ.

We impose a no-slip boundary condition on the wall of the tube, $\mathbf{u}(x, b) = \mathbf{u}(x, -b) = 0, x \in [0, L]$ and the following natural boundary conditions at the inlet and the outlet:

$$\mathbf{T}(\mathbf{u}, p)(0, y) \cdot \mathbf{n} = -P_0 \mathbf{n}, \quad \mathbf{T}(\mathbf{u}, p)(L, y) \cdot \mathbf{n} = -P_L \mathbf{n}, \quad y \in [-b, b],$$

Remark 3.1. In absence of stent (namely if $r_\gamma = 0$), the solution to this problem is the standard Poiseuille flow with a linear decreasing pressure and a parabolic velocity profile. Of course, this holds not true if $r_\gamma > 0$, since, in particular, if the pressure was constant over a tube section, then the fourth equation in (2) would yield a flat velocity profile on the interface γ (which is incompatible with the parabolic profile of Poiseuille flows). Nevertheless, as a first approximation, if we assume that a Poiseuille flow is established in Ω_1 and Ω_2 then, we readily obtain

$$\bar{u} \quad = \quad -\frac{b^2}{3\mu L_1}(P_1 - P_0) \quad = \quad -\frac{1}{r_\gamma}(P_2 - P_1) \quad = \quad -\frac{b^2}{3\mu L_2}(P_L - P_2),$$

with $\bar{u} = \frac{1}{2b}\int_{-b}^{b} u(y)dy$, and $P_1 = P(L_1^-)$, $P_2 = P(L_1^+)$. Thus introducing $R_i = \frac{3\mu L_i}{b^2}, i = 1, 2$, we have

$$P_0 - P_L = (R_1 + r_\gamma + R_2)\bar{u}. \tag{25}$$

In particular this relation can be used to evaluate experimentally the parameter r_γ of real stents. Our computations have been performed with realistic values obtained in this way.

The following parameters are considered for the numerical simulations. The dimensions of the tube are $L_1 = L_2 = 4\,cm$, $2b = 0.4\,cm$, the viscosity is $\mu = 0.04\,g/(cms)$ and the stent resistivity is $r_\gamma = 100\,g/(cm^2 s)$. We impose a constant pressure drop $\Delta P = 1000\,g/(cms^2)$ in a transient simulation, and wait for the stationary state to be reached.

According to Remark 3.1, an approximation of the solution is obtained by assuming a Poiseuille flow before and after the stent. The corresponding mean flow and the pressure jump at the interface are readily given by:

$$\phi^{QP} = \int_{-b}^{b} u(y)dy \approx 3.226\ cm^3\,s^{-1}, \qquad \Delta P_\gamma^{QP} = P_1 - P_2 \approx 806.5\ g\,cm^{-1}s^{-2}. \tag{26}$$

Since no analytical solution is available for this test-case, we compare the mean values of the numerical results with this approximated solution.

The mesh is made of structured quadrangles. It is supposed to be conforming at the interface, *i.e.* the interface is made of edges of the global mesh. It is possible to introduce, or not, a fissure in the mesh. On the fissure, each geometrical point is associated to two vertices in the mesh. Such a fissured mesh allows *discontinuous* pressure on the interface.

In Table 1, we summarize the results obtained with different types of discretization spaces:

- stable finite elements: Q_2 velocity, and Q_1 pressure (continuous) or P_1 pressure (discontinuous);
- stabilized finite element: Q_1 velocity, and Q_1 pressure (continuous).

We refer to [19] or [13] for the precise definitions of these spaces. In the first column of Table 1, the mesh has no fissure on the interface. Thus, the pressure is discontinuous on the interface only with the Q_2/P_1 pair of finite element. In the second column, the mesh contains a fissure at the interface. In this case, the pressure is always discontinuous at the interface and, as far as the Q_1/Q_1 pair is concerned, the stabilization includes the terms introduced in Section 2.2. The qualitative convergence behavior with respect to the mesh refinement is also provided in these different cases.

	No Fissure			Fissure		
$p_h\vert_\gamma$	C^o	C^o	Disc	Disc	Disc	Disc
Spaces	Q_1/Q_1	Q_2/Q_1	Q_2/P_1	Q_1/Q_1	Q_2/Q_1	Q_2/P_1
Convergence	no CV	slow	*OK*	*OK*	*OK*	*OK*

Table 1: Effect of the continuity of the pressure at the interface over the h convergence, using different discretization spaces.

In Figure 7, we show the velocity around the interface. The velocity profile is almost parabolic in the tube, except near the resistive interface, where it tends to be flat (see Remark 3.2). In Figure 8, Left, the pressure profile along the axis $y = 0$ of the tube is reported. The pressure is almost linearly varying in the subdomains, with a strong pressure drop across the interface. In Figure 8, Right, one can see the evolution of the outlet flux $\phi = \int_{-b}^{b} u(y)dy$ as a function of time, until it reaches the stationary state. In both cases, we have drawn (straight lines labelled by "Ref QP") the result predicted by the "quasi-Poiseuille" approximation (see (26) and Remark 3.2).

When the pressure is approximated *continuously* at the interface, the results are poor: the flux computed in this example is almost twice as large as the correct value, even for a very refined mesh. We note that with the same stabilized Q_1/Q_1 elements, but with a fissure at the interface, a correct solution is computed using the coarsest mesh.

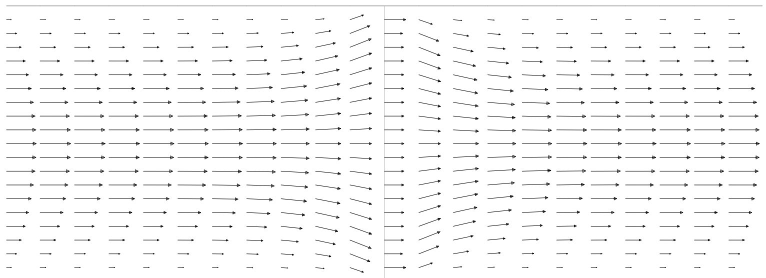

Figure 7: Velocity with a resistive surface ($r_\gamma = 100$) in a 2D tube. Discretization: Q_1/Q_1 with a fissure. Velocity scale: from 0 up to 11.8. For picture purposes, the mesh presented in this figure is quite coarse.

Figure 9 shows the results for the Q_2/Q_1 discretization (Left) and the Q_2/P_1 discretization (Right). With the Q_2/Q_1 elements, the pressure lies in a continuous space of approximation, and thus one needs either to refine a lot the mesh, or to introduce a fissure in the mesh, to compute the correct solution. With the Q_2/P_1 elements, as the pressure is element-wise discontinuous, the solution is correctly computed with a coarse mesh. There exists a slight discrepancy between the flux obtained from the "quasi-Poiseuille" flow and the flux computed with the model due to the fact that the "quasi-Poiseuille" flow is *not* a solution of the model problem.

In conclusion, this test-case shows that it seems to be necessary to use a discontinuous approximation of the pressure across the stent, at least when realistic values of resistivity are used. Once a fissure is created on the stent, our stabilized Q_1/Q_1 method gives results which are similar to the stable Q_2/P_1 finite element. In the 3D simulations presented in the next section, we will limit ourselves to stabilized tetrahedral P_1/P_1 finite elements.

Remark 3.2. In the context of homogenization, Sanchez-Palencia [23] and Conca,[10, 11], studied the behavior of a flow through a planar sieve. Conca proved that the flow, away from the sieve, tends to satisfy a Stokes problem, with a constant velocity on the sieve. Some numerical solutions in the vicinity of the sieve were presented in [12]. Our numerical experiments show a very similar behavior (Figure 7).

3.3 Bifurcation in a realistic 3D geometry

We present some results that are carried out on a realistic aneurysm geometry. Two cases are considered: a rigid arterial wall, or an elastic arterial wall. In all cases, the stent is considered rigid, and is represented by the model (1). The fluid-structure interaction between the blood

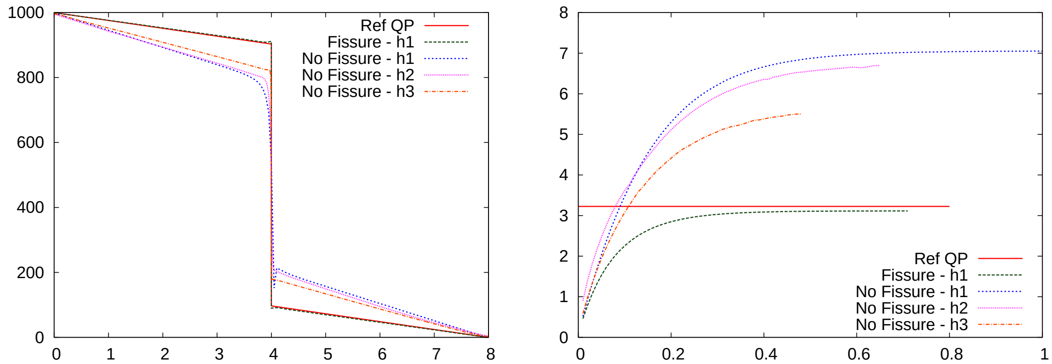

Figure 8: Tube 2d with a stent: Influence of the mesh refinement on the solution, for the Q_1/Q_1 discretization ($r_\gamma = 100$). Left: pressure as a function of x. Right: out flux as a function of time. In the two figures, the first curve represents the "quasi-Poiseuille" flow approximation (*"Ref QP"*). The second curve represents the numerical solution on a coarse mesh with a discontinuous pressure approximation; the pressure is almost superimposed on the *"Ref QP"* curve . For the three remaining curves, the pressure was approximated continuously. When $h = h1$ (second and third curve), the mesh is regular and contains 3200 cells. When $h = h2$ (fourth curve) (resp. $h = h3$ (fifth curve)), the mesh is locally refined around the interface and contains 6400 (resp. 12800) cells.

and the artery that occurs when the arterial wall is compliant, is solved via a quasi-Newton algorithm, see [17].

3.3.1 Mesh considerations

The surface of a human cerebral artery bifurcation containing a huge terminal aneurysm (about 10 mm wide) was obtained by medical imaging techniques and meshed using Yams, [16]. Then from the surface mesh a 3D mesh was created using GHS3D[1]. Some computations have already been achieved with this mesh, [22, 18].

An idealized stent is inserted in the primary surface mesh, see Figure 10. For simplicity, we use a crude geometry for the stent: it is represented by three planar surfaces that intersect the entrance of the two branches and of the aneurysm, thus decomposing the domain into four subdomains: the trunk of the artery called Ω_{tr}, the two branches Ω_{br1} and Ω_{br2} and the aneurysm Ω_{an}. Each subdomain surface is meshed in quadrangles using Yams, in order to use a shell structure code (based on Modulef[2]) for the arterial wall. Each subdomain are then meshed in tetrahedra in a conforming way using GHS3D, and glued together leaving a fissure at the interfaces. Finally, a 3D conforming mesh in tetrahedra with internal fissures representing the stent is created. We obtain also a quadrangular surface mesh whose vertices are the ones of the skin of the 3D mesh.

[1]See http://www-c.inria.fr/Eric.Saltel/gamma/ghs3d
[2]See http://www-rocq.inria.fr/modulef/

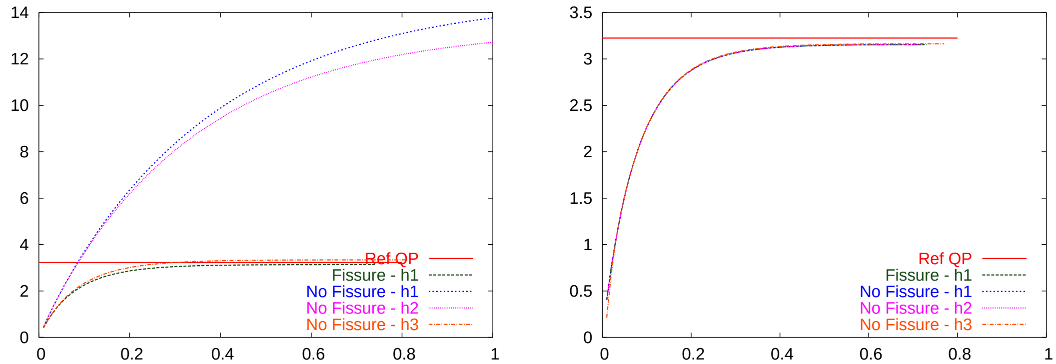

Figure 9: Tube 2d with a stent: Influence of the mesh refinement on the solution, for the Q_2/Q_1 and the Q_2/P_1 discretizations. $r_\gamma = 100$. Left and right: out flux as a function of time. Left: Q_2/Q_1 elements. Right: $Q_2/P1$ elements. In the two figures, the first curve represents the "quasi-Poiseuille" flow approximation (*"Ref QP"*). When $h = h1$ (second and third curves) (resp. $h = h2$ (fourth curve)), the mesh is regular and contains 800 (resp. 3200) cells. When $h = h3$ (fifth curve), the mesh is locally refined around the interface and still contains 3200 cells. Left: with no fissure at the interface, the pressure is approximated continuously, and one needs to refine the mesh a lot to obtain the correct solution. A good solution can be computed at a much cheaper cost with a fissured mesh. Right: all curves are superimposed. The pressure lies in a discontinuous space and therefore one can catch the discontinuity without extreme mesh refinement, nor a fissure in the mesh.

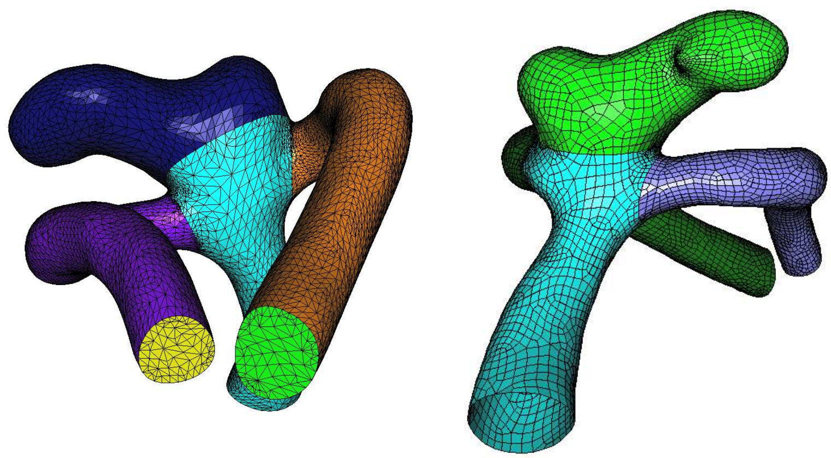

Figure 10: Mesh of the terminal aneurysm. Each subdomain is depicted with a different color. Left: fluid mesh, Right: quadrangular shell mesh. Different view points. The stent separates the trunk artery (vertical inlet branch), from the two outlet branches , and from the aneurysm (top part). Visualization with medit, [15].

3.3.2 Description of the problem

Rigid wall In the case of a rigid arterial wall, the computation is performed in different configurations over 3 cardiac cycles of period $T = 0.8s$. Problem (1) is completed with the following boundary conditions: we impose a pressure wave at the inlet Γ_{in} (Neumann boundary conditions) and a flow–pressure relation simulating the rest of the arterial circuit is imposed at the outlets $\Gamma_{out,1}$ and $\Gamma_{out,2}$. On the rest of the boundary Γ_0, a no-slip condition is imposed:

$$\begin{array}{rcll} \mathbf{T}(\mathbf{u},p)\cdot\mathbf{n}(x,t^n) & = & -p_{in}(t^n) & \text{on } \Gamma_{in}, \\ \mathbf{T}(\mathbf{u},p)\cdot\mathbf{n}(x,t^n) & = & R_{out}\phi_i(t^n) & \text{on } \Gamma_{out,i}, i=1,2, \\ \mathbf{u} & = & 0 & \text{on } \Gamma_0, \end{array} \tag{27}$$

where p_{in} is a given pressure function plotted in Figure 11, $\phi_i = \int_{\Gamma_{out,i}} \mathbf{u}\cdot\mathbf{n}$ is the out flux, and the resistivity R_{out} was taken equal to 10^5. The pressure varies over a $5.3\;10^4\;g/(cm\,s^2) \approx 40\;mm\,Hg$ amplitude, which corresponds to typical pressure drops in physiological conditions (between 80 and 120 $mm\,Hg$).

The viscosity is $\mu = 0.035\,g\,(cm\,s)^{-1}$, the fluid density is $\rho_f = 1\,g/cm^3$. The time step was taken equal to $0.01s$. We used a Lagrange P_1/P_1 stabilized finite elements for the space discretization. Thanks to the fissures in the mesh, we let the pressure be discontinuous at the resistive interfaces, whereas the velocity is continuous.

Elastic wall All the remarks made in the rigid wall case still apply, except that the computation is made over 1 cardiac cycle and a time step ten times smaller was taken ($dt = 10^{-3}$).

Concerning the structure, a non-linear shell model is used, see for instance [6]. The Young modulus is $E = 6\;10^6\;dyn\,cm^2$, the Poisson coefficient is $\nu = 0.3$ and the thickness is $0.025\,cm$ (about one tenth of the artery diameter). For simplicity, the shell is assumed to be clamped at its boundaries.

3.3.3 Results

In the different cases studied (see Table 2 for the rigid wall case and Table 3 for the moving wall case), we changed the resistivity of the stent, in order to assess the impact of the stent on the blood flow. We call r_{an} the resistivity the stent portion located at the entrance of the aneurysm, r_{br} the resistivity of the stent portion located at the entrance of the 2 branches. In the case 0, there is no stent. In the other ones, the stent has *a priori* a non-homogeneous permeability: it is more resistive at the entrance of the aneurysm than at the entrance of the branches.

We present the solution at the systole in three main configurations: without any stent (test case 0), and when the aneurysm resistivity is twice as large as the ones at the entrance of the branches: stent with the resistivities $r_{an} = 50$, $r_{br} = 20$ (test case 4), stent with $r_{an} = 100$, $r_{br} = 50$ (test case 10).The results are summarized in Tables 2 and 3.

In Figure 12, the peak pressure at the systole is depicted. It has to be noticed that the stent induces a pressure jump at the interfaces, notably between the trunk and the branches. When the arterial wall is compliant, the arteries and the aneurysm are slightly dilated under the pressure constraint, as expected. The pressure inside the aneurysm is not significantly modified by the stent in both the rigid and moving wall cases.

In Figure 13, the peak velocity along the trunk of the artery and inside the aneurysm is shown. Whereas the maximum velocity in the trunk is not really affected by a stent (it reaches its maximum value near the location where the trunk is the thinnest), the fluid velocity in the aneurysm is considerably reduced by the stent, as expected. A vortex in the aneurysm still exists for a resistivity $r_{an} = 50$, but can hardly be seen. The velocity in the aneurysm is depicted in

Case	r_{an}	r_{br}	$\|\|\phi\|\|_{\Gamma_{in},\infty}$	$\|\|\phi\|\|_{\Gamma_{out,1},\infty}$	$\|\|\phi\|\|_{\Gamma_{out,2},\infty}$	$\frac{\|\|\mathbf{u}\|\|_{\Omega_{an},\infty}}{\|\|\mathbf{u}\|\|_{\Omega_{tr},\infty}}$	$\|\|\nabla \times \mathbf{u}\|\|_{\Omega_{an},2}$	$\|\|WSS\|\|_{\partial\Omega_{an},2}$
0	0	0	1.02	0.513	0.504	69.9%	61.7	11.6
1	50	1	1.01	0.513	0.504	23.4%	14.1	2.93
2	50	5	1.01	0.513	0.503	23.3%	14.0	2.90
3	50	10	1.01	0.512	0.502	23.2%	13.9	2.88
4	50	20	1.01	0.51	0.5	23.0%	13.7	2.82
5	50	50	1.0	0.505	0.494	22.6%	13.2	2.70
6	100	1	1.02	0.513	0.504	12.7%	7.3	1.61
7	100	5	1.02	0.513	0.503	12.7%	7.3	1.60
8	100	10	1.01	0.512	0.502	12.7%	7.2	1.59
9	100	20	1.01	0.51	0.5	12.5%	7.1	1.56
10	100	50	1.0	0.506	0.495	12.2%	6.9	1.49
11	100	100	0.98	0.498	0.486	11.9%	6.5	1.40
12	200	50	1.0	0.506	0.495	6.5%	3.5	0.80
13	200	100	0.98	0.498	0.486	6.3%	3.4	0.75

Table 2: Different test-cases for the **rigid arterial wall** computations: stent resistivities in the aneurysm r_{an}, and in the branches r_{br} ($\frac{g}{cm^2 s}$), peak inflow ($\frac{cm^3}{s}$), peak outflows at the two outlets, ratio of the maximum velocity in the aneurysm over the maximum velocity in the trunk, L^2 norm of the vorticity in the aneurysm and of the wall shear stress at the wall of the aneurysm.

Case	r_{an}	r_{br}	$\|\|\phi\|\|_{\Gamma_{in},\infty}$	$\|\|\phi\|\|_{\Gamma_{out,1},\infty}$	$\|\|\phi\|\|_{\Gamma_{out,2},\infty}$	$\frac{\|\|\mathbf{u}\|\|_{\Omega_{an},\infty}}{\|\|\mathbf{u}\|\|_{\Omega_{tr},\infty}}$	$\|\|\nabla \times \mathbf{u}\|\|_{\Omega_{an},2}$	$\|\|WSS\|\|_{\partial\Omega_{an},2}$
0	0	0	1.05	0.523	0.513	73.8%	71.8	12.9
4	50	20	1.04	0.520	0.509	22.7%	14.8	2.80
10	100	50	1.03	0.516	0.503	12.9%	7.6	1.47

Table 3: Different test-cases for the **elastic arterial wall** computations: stent resistivities in the aneurysm r_{an}, and in the branches r_{br} ($\frac{g}{cm^2 s}$), peak inflow ($\frac{cm^3}{s}$), peak outflows at the two outlets, ratio of the maximum velocity in the aneurysm over the maximum velocity in the trunk, L^2 norm of the vorticity in the aneurysm and of the wall shear stress at the wall of the aneurysm.

Figure 14: as expected, it decreases when the aneurysm resistivity r_{an} increases (different scales in each picture), see also the Tables 2 and 3: the ratio of maximum velocities in the aneurysm and in the trunk is reduced from 70% (no stent) to 23% when $r_{an} = 50$, to 13% when $r_{an} = 100$, and to 6% when $r_{an} = 200$. See also the Figure 16, where the maximum velocity in the aneurysm as a function of time is plotted. The velocity in the aneurysm is slightly larger when the computation takes into account the compliance of the wall.

In Figure 15, the wall shear stress at the wall of the aneurysm is plotted. Two different scales are used, the one with no stent being five times larger than the other. The maximum values of the wall shear stress seem to appear at the same locations in all cases. No significant differences can be noticed between the rigid and moving wall computations.

As one would expect, when a given pressure drop is imposed, the flow in the artery slightly decreases as the stent resistivity of the branches increases. This is normal as the overall resistivity of the domain to the fluid is increased by the stent. Other numerical experiments show that this effect can be quite important, in particular when the pressure imposed p_{in} is smaller[3]. One can note that the aneurysm stent has little influence over the global flow. In Figure 11, the input flow as a function of time is depicted over one period. We show in Figure 16 the L^2 norm of the wall shear stress on the wall of the aneurysm as a function of time. It is dramatically reduced by the stent. The vorticity inside the aneurysm shows a similar behavior. Finally, in Figure 17, we compared the maximum velocity in the aneurysm and the wall shear stress in the rigid and moving wall cases. There are no significant differences, except that, when the wall is compliant, the values are a bit larger.

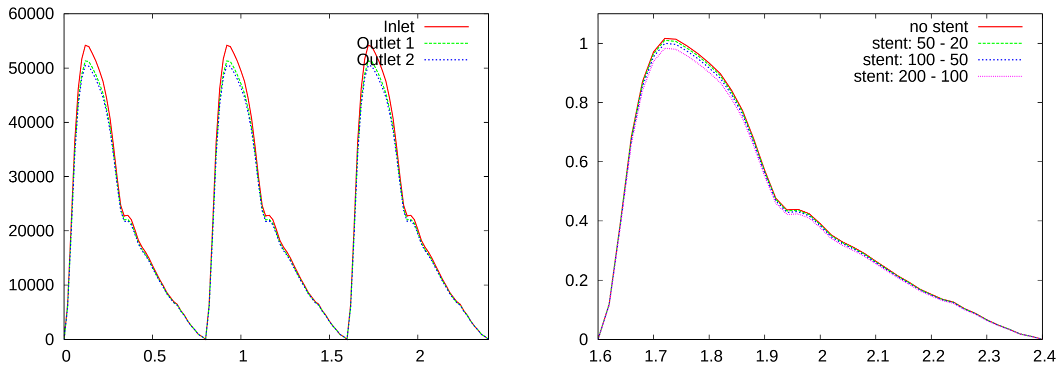

Figure 11: Left: input pressure in all test-cases (top curve), and output pressure in the test case 0 (no stent) at $\Gamma_{out,1}$ (middle curve) and $\Gamma_{out,2}$ (lowest curve). A slight asymmetry can be noticed. Scale: $[0; 6E4]$. Right: input flow (scale $[0; 1.1]$) as a function of time for one cardiac cycle. Curves, from top to bottom: test cases 0 (no stent), 4, 10, 13. The flow decreases very slowly when the resistivity increases (which is a desirable feature).

3.3.4 Discussion

The numerical experiment shows that the presence of a stent with some realistic resistivity properties considerably reduces the velocity in the aneurysm, and thus the vorticity and the wall

[3]In the same configuration, for a pressure p_{in} about ten times smaller ($\approx 5mm\,Hg$), an outlet resistivity $R_{out} = 1E4$ and a resistance $r_{br} = 50$, a flow reduction of about 10% was observed with the stent.

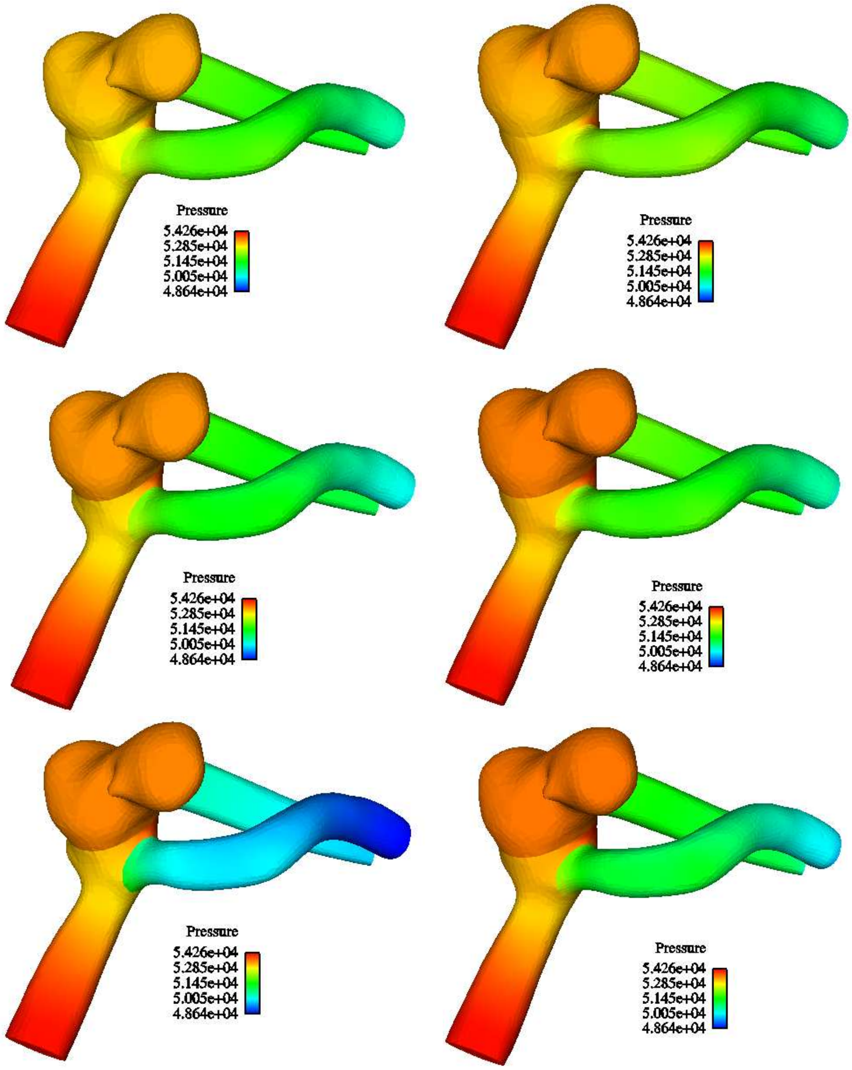

Figure 12: Systolic pressure for different resistivities, and with rigid or moving arterial walls. Scale: $[4.8\ 10^4, 5.4\ 10^4]$. Left column: rigid arterial wall. Right column: moving wall. From Top to Bottom: no stent, test case 4 (stent with the resistivities: $r_{an} = 50,\ r_{br} = 20$), test case 10 ($r_{an} = 100,\ r_{br} = 50$).

shear stress on the wall of the aneurysm. Thus, one can predict that a blood clot could be created rapidly in the aneurysm, thanks to the stent. Besides, the global blood flow does not seem to be too much perturbed by the stent, out of the aneurysm: in particular, the outflow in physiological conditions remains almost unchanged. The results did not change significantly between the rigid wall case and the moving wall case, thus, in this configuration, it does not seem necessary to perform the full fluid-structure interaction computation to obtain reasonable results.

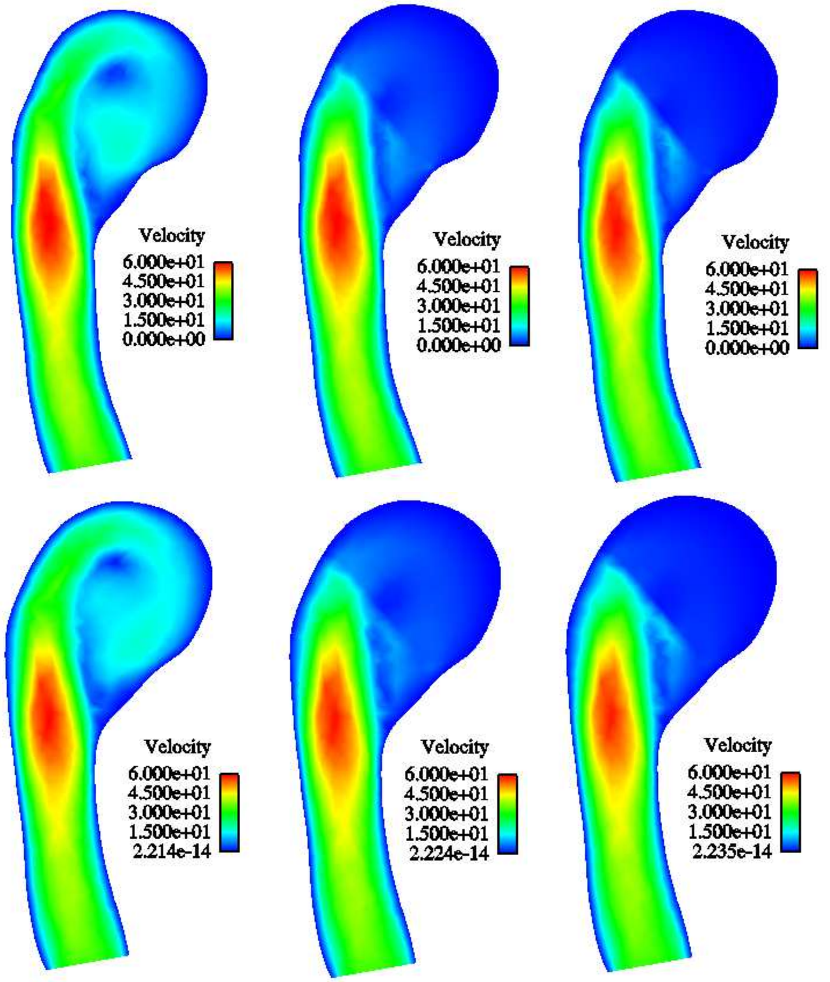

Figure 13: Systolic velocity in a planar section of the trunk and the aneurysm. The cut plane is located approximately along the trunk axis, and is perpendicular to the two entrances into the branches. The location of the aneurysm stent, if present, can be guessed as it limits the low velocity zone and the trunk region. Scale: $[0, 60]$. Top: rigid arterial wall. Bottom: moving wall. From Left to Right: no stent, test cases 4 ($r_{an} = 50,\ r_{br} = 20$), 10 ($r_{an} = 100,\ r_{br} = 50$).

4 Conclusions and perspectives

We have presented a model to represent the interaction between a stent and the blood flow in arteries. Our purpose was to build a model simple enough and easily parametrized with the available data. We have modelled the stent as a rigid dissipative interface which interacts with an incompressible fluid governed by the Navier-Stokes equations. This interface creates a jump of the normal stress that is proportional to the velocity. The proportionality coefficient is a resistivity that can be determined by measurements. The jump of normal stress induces a discontinuity

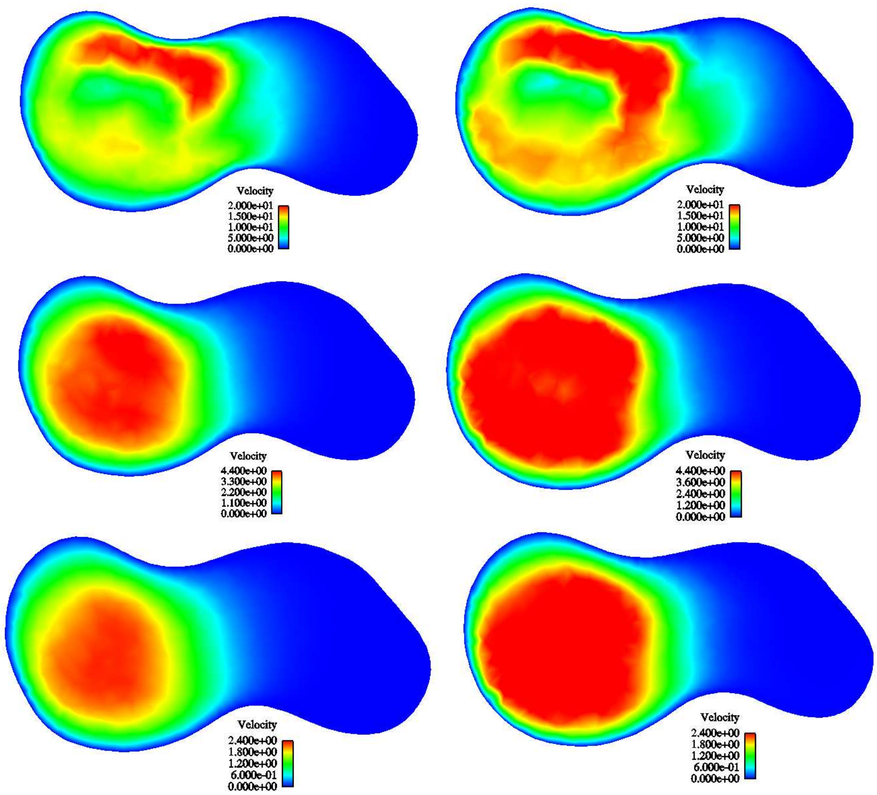

Figure 14: Systolic velocity in a planar section of the aneurysm. The cut plane is located approximately at the middle of the aneurysm, and is parallel to entrance of the aneurysm. Left column: rigid arterial wall. Right column: moving wall. From Top to Bottom: no stent (scale: $[0, 20]$), test case 4 ($r_{an} = 50$, $r_{br} = 20$, scale $[0, 4.4]$), test case 10 ($r_{an} = 100$, $r_{br} = 50$, scale: $[0, 2.4]$).

of the pressure that has to be correctly approximated: the discrete pressure space must be discontinuous at the interface. A convergence analysis is presented in the stationary linear case for a stabilized finite element method, involving a discontinuous pressure at the interface. Some simple two dimensional numerical tests have confirmed the theoretical convergence rate. Other numerical experiments have been presented in a realistic three dimensional saccular terminal aneurysm. Given a fixed pressure drop imposed at the boundaries, the stent acts as a resistance that only slightly reduces the flow exiting the domain. The stent decreases the velocities and the vorticity in the aneurysm, and tends to reduce also the aneurysm wall stresses. This indicates that the process of thrombosis might occur in the aneurysm, as desired.

The work could be improved in several ways. First, more realistic stent geometries could used. Second, better outflow boundary conditions could be devised, using either an impedance [28] or a network of 1D models [21, 14]. Finally, it would be interesting to take into account a model of coagulation in the aneurysm, following for instance [29].

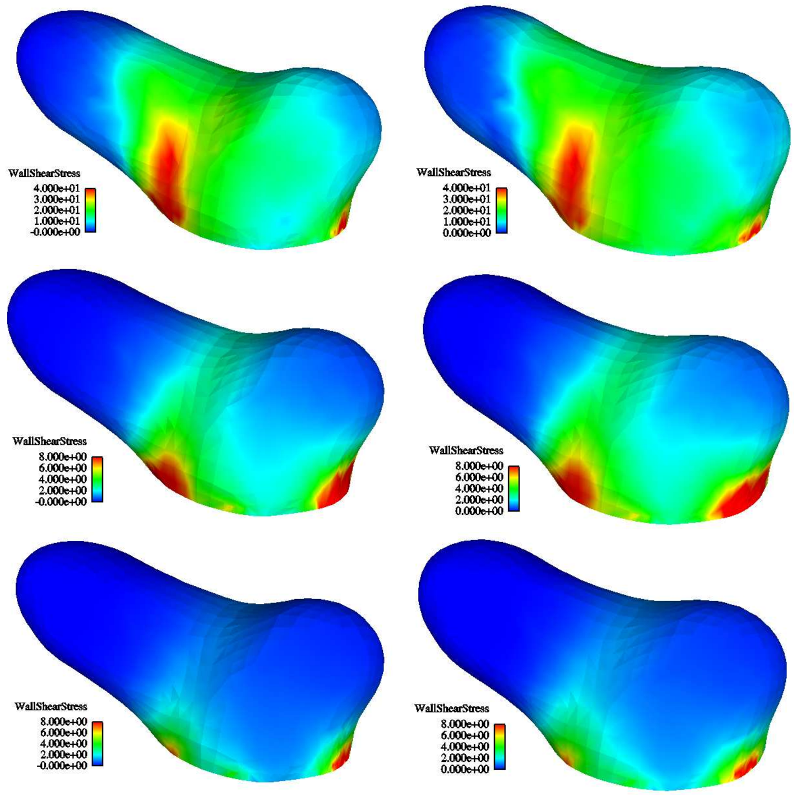

Figure 15: Systolic wall shear stress on the boundary of the aneurysm. Left column: rigid arterial wall. Right column: moving wall. From Top to Bottom: no stent (scale: $[0, 40]$), test case 4 ($r_{an} = 50,\ r_{br} = 20$, scale $[0, 8]$), test case 10 ($r_{an} = 100,\ r_{br} = 50$, scale: $[0, 8]$).

Acknowledgement: This work was partially supported by Cardiatis. The authors thank N. Frid and P. Gruffaz (Cardiatis) who proposed this study and whose encouragements and constructive suggestions were of great help.

References

[1] G. Allaire. Homogenization of the Navier-Stokes equations in open sets perforated with tiny holes. II. Noncritical sizes of the holes for a volume distribution and a surface distribution of holes. *Arch. Rational Mech. Anal.*, 113(3):261–298, 1991.

[2] J.L. Berry, A. Santamarina, J.E. Jr. Moore, S. Roychowdhury, and W.D. Routh. Experimental and computational flow evaluation of coronary stents. *Annals of Biomedical Engineering*, 28:386–398, 2000.

[3] F. Brezzi and M. Fortin. *Mixed and Hybrid Finite Element Methods.* Springer-Verlag, Berlin, 1991.

[4] A. Brillard. Asymptotic flow of a viscous and incompressible fluid through a plane sieve. In *Progress in partial differential equations: calculus of variations, applications (Pont-à-*

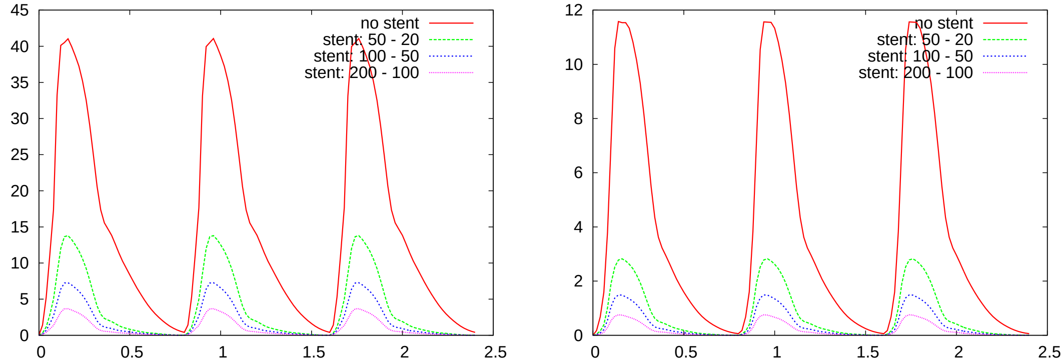

Figure 16: Rigid wall computation. Left: maximum velocity in the aneurysm (scale $[0; 45]$) as a function of time. Right: L^2 norm of the wall shear stress on the aneurysm wall (scale $[0; 12]$) as a function of time. Curves, from top to bottom: test cases 0 (no stent), 4, 10, 13.

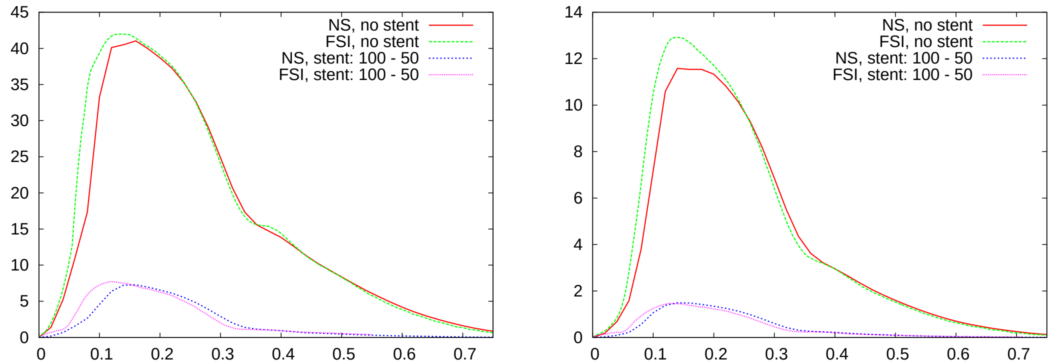

Figure 17: Comparison between rigid and moving arterial walls. Left: maximum velocity in the aneurysm (scale $[0; 45]$) as a function of time. Right: L^2 norm of the wall shear stress on the aneurysm wall (scale $[0; 14]$) as a function of time. Curves, from top to bottom: test cases 0 (no stent) with rigid (*"NS"*) and moving wall (*"FSI"*), 10 with rigid and moving wall.

Mousson, 1991), volume 267 of *Pitman Res. Notes Math. Ser.*, pages 158–172. Longman Sci. Tech., Harlow, 1992.

[5] E. Burman and P. Hansbo. Edge stabilization for the generalized Stokes problem: a continuous interior penalty method. *Comput. Methods Appl. Mech. Engrg.*, 195(19-22):2393–2410, 2006.

[6] D. Chapelle and K. J. Bathe. *The finite element analysis of shell - Fundamentals.* Springer-Verlag, 2004.

[7] P.G. Ciarlet. *The finite element method for elliptic problems*, volume 40 of *Classics in Applied Mathematics.* Society for Industrial and Applied Mathematics (SIAM), Philadelphia, PA, 2002. Reprint of the 1978 original [North-Holland, Amsterdam; MR0520174 (58 #25001)].

[8] P. Clément. Approximation by finite element functions using local regularization. *Rev. Française Automat. Informat. Recherche Opérationnelle Sér. Rouge Anal. Numér.*, 9(R-2):77–84, 1975.

[9] R. Codina and J. Blasco. A finite element formulation for the Stokes problem allowing equal velocity-pressure interpolation. *Comput. Methods Appl. Mech. Engrg.*, 143(3-4):373–391, 1997.

[10] C. Conca. Étude d'un fluide traversant une paroi perforée. I. Comportement limite près de la paroi. *J. Math. Pures Appl. (9)*, 66(1):1–43, 1987.

[11] C. Conca. Étude d'un fluide traversant une paroi perforée. II. Comportement limite loin de la paroi. *J. Math. Pures Appl. (9)*, 66(1):45–70, 1987.

[12] C. Conca and M. Sepúlveda. Numerical results in the Stokes sieve problem. *Rev. Internac. Métod. Numér. Cálc. Diseñ. Ingr.*, 5(4):435–452, 1989.

[13] A. Ern and J.-L. Guermond. *Theory and practice of finite elements*, volume 159 of *Applied Mathematical Sciences*. Springer-Verlag, New York, 2004.

[14] L. Formaggia, J.-F. Gerbeau, F. Nobile, and A. Quarteroni. On the coupling of 3D and 1D Navier-Stokes equations for flow problems in compliant vessels. *Comput. Methods Appl. Mech. Engrg.*, 191(6-7):561–582, 2001.

[15] P. Frey. Medit: an interactive mesh visualisation software. Technical report 0253, Inria, Rocquencourt, France, Dec. 2001.

[16] P. Frey. Yams: A fully automatic adaptive isotropic surface remeshing procedure. Technical report 0252, Inria, Rocquencourt, France, Nov. 2001.

[17] J.-F. Gerbeau and M. Vidrascu. A quasi-Newton algorithm based on a reduced model for fluid structure problems in blood flows. *M2AN Math. Model. Numer. Anal.*, 37(4):631–647, 2003.

[18] J.-F. Gerbeau, M. Vidrascu, and P. Frey. Fluid-structure interaction in blood flows on geometries coming from medical imaging. *Computers and Structure*, 83(2–3):155–165, 2005.

[19] V. Girault and P.-A. Raviart. *Finite element methods for Navier-Stokes equations*, volume 5 of *Springer Series in Computational Mathematics*. Springer-Verlag, Berlin, 1986. Theory and algorithms.

[20] T.J.R. Hughes, L.P. Franca, and M. Balestra. A new finite element formulation for computational fluid dynamics : V. circumventing the Babuska-Brezzi condition : a stable Petrov-Galerkin formulation of the Stokes problem accommodating equal-order interpolations. *Comp. Meth. App. Mech. Eng.*, 59:85–99, 1986.

[21] A. Quarteroni and L. Formaggia. Mathematical modelling and numerical simulation of the cardiovascular system. In *Handbook of numerical analysis. Vol. XII*, Handb. Numer. Anal., XII, pages 3–127. North-Holland, Amsterdam, 2004.

[22] S. Salmon, M. Thiriet, and J.-F. Gerbeau. Medical image-based computational model of pulsatile flow in saccular aneurisms. *M2AN Math. Model. Numer. Anal.*, 37(4):663–679, 2003.

[23] E. Sánchez-Palencia. Problèmes mathématiques liés à l'écoulement d'un fluide visqueux à travers une grille. In *Ennio De Giorgi colloquium (Paris, 1983)*, volume 125 of *Res. Notes in Math.*, pages 126–138. Pitman, Boston, MA, 1985.

[24] D. A. Steinman, J. S. Milner, C. J. Norley, S. P. Lownie, and D. W. Holdsworth. Image-based computational simulation of flow dynamics int a giant intracranial aneurysms. *Am. J. Neuroradiol.*, 24:559–566, 2003.

[25] G.R. Stuhne and D.A. Steinman. Finite-element modeling of the hemodynamics of stented aneurysms. *J. Biomech. Eng.*, 126(3):382–387, 2004.

[26] V. Thomée. *Galerkin finite element methods for parabolic problems*, volume 25 of *Springer Series in Computational Mathematics*. Springer-Verlag, Berlin, second edition, 2006.

[27] L. Tobiska and V. Verfurth. Analysis of a streamline diffusion finite element method for the stokes and navier–stokes equations. *SIAM Journal on Numerical Analysis*, 33(1):107–127, 1996.

[28] I.E. Vignon-Clementel, C.A. Figueroa, K.E. Jansen, and C.A. Taylor. Outflow boundary conditions for three-dimensional finite element modeling of blood flow and pressure in arteries. *Comput. Methods Appl. Mech. Engrg.*, 195(29-32):3776–3796, 2006.

[29] N.T. Wang and A.L. Fogelson. Computational methods for continuum models of platelet aggregation. *J. Comput. Phys.*, 151(2):649–675, 1999.

Unité de recherche INRIA Rocquencourt
Domaine de Voluceau - Rocquencourt - BP 105 - 78153 Le Chesnay Cedex (France)

Unité de recherche INRIA Futurs : Parc Club Orsay Université - ZAC des Vignes
4, rue Jacques Monod - 91893 ORSAY Cedex (France)
Unité de recherche INRIA Lorraine : LORIA, Technopôle de Nancy-Brabois - Campus scientifique
615, rue du Jardin Botanique - BP 101 - 54602 Villers-lès-Nancy Cedex (France)
Unité de recherche INRIA Rennes : IRISA, Campus universitaire de Beaulieu - 35042 Rennes Cedex (France)
Unité de recherche INRIA Rhône-Alpes : 655, avenue de l'Europe - 38334 Montbonnot Saint-Ismier (France)
Unité de recherche INRIA Sophia Antipolis : 2004, route des Lucioles - BP 93 - 06902 Sophia Antipolis Cedex (France)

Éditeur
INRIA - Domaine de Voluceau - Rocquencourt, BP 105 - 78153 Le Chesnay Cedex (France)
http://www.inria.fr
ISSN 0249-6399